Spring 2017

Multimodal evaluation of local and whole-joint cartilage changes in an in vivo animal model

David James Heckelsmiller
University of Iowa

MULTIMODAL EVALUATION OF LOCAL AND WHOLE-JOINT CARTILAGE CHANGES IN AN IN VIVO ANIMAL MODEL

by

David James Heckelsmiller

A thesis submitted in partial fulfillment
of the requirements for the Master of Science
degree in Biomedical Engineering in the
Graduate College of
The University of Iowa

May 2017

Thesis Supervisor: Assistant Professor Jessica E. Goetz

Graduate College
The University of Iowa
Iowa City, Iowa

CERTIFICATE OF APPROVAL

_____

MASTER'S THESIS

_____

This is to certify that the Master's thesis of

David James Heckelsmiller

has been approved by the Examining Committee for
the thesis requirement for the Master of Science degree
in Biomedical Engineering at the May 2017 graduation.

Thesis Committee: _____
Jessica E. Goetz, Thesis Supervisor

_____
Nicole M. Grosland

_____
Douglas R. Pedersen

_____
Dan R. Thedens

To my parents

"It is not the critic who counts; not the man who points out how the strong man stumbles, or where the doer of deeds could have done them better. The credit belongs to the man who is actually in the arena, whose face is marred by dust and sweat and blood; who strives valiantly; who errs, who comes short again and again, because there is no effort without error and shortcoming; but who does actually strive to do the deeds; who knows great enthusiasms, the great devotions; who spends himself in a worthy cause; who at the best knows in the end the triumph of high achievement, and who at the worst, if he fails, at least fails while daring greatly, so that his place shall never be with those cold and timid souls who know neither victory nor defeat."

Theodore Roosevelt
The Man in the Arena

ACKNOWLEDGEMENTS

Thank you to the students and staff of the Iowa Orthopedic Biomechanics Lab for providing guidance and mentoring during the course of my journey as a graduate student. Also, thanks to my teammates, my brother, and my sister for motivating and inspiring me daily. Thanks to my Aunt for providing advice and support throughout my time in Iowa City. Finally, thanks to my parents! This work has been funded by the National Institute of Arthritis and Musculoskeletal and Skin Diseases, a subsidiary of the National Institutes of Health (#AR055533).

ABSTRACT

Osteoarthritis is a chronic, deleterious disease of the joints. It currently affects nearly 25 million Americans. Clinically, osteoarthritis presents as joint pain and verified by radiographic evidence of joint space narrowing. Unfortunately, symptomatic osteoarthritis describes the later stages of disease, at which point irreversible cartilage and bone damage has occurred. Cross-sectional imaging modalities offer the promise of visualizing early features of disease, enabling the development and evaluation of interventions to forestall or prevent degenerative change. Modalities of clinical interest include magnetic resonance imaging (MRI) and multi-detector computed tomography (MDCT).

The following work describes the efficacy of MRI-derived measures for the identification and accurate quantification of local and whole joint changes in articular cartilage thickness changes *in vivo*. This was performed as part of a study investigating the diagnostic potential of clinical morphometric and compositional MRI to identify early features of osteoarthritis in a large animal model of traumatic knee joint injury. Surgically induced trauma consisted of a partial medial meniscectomy and blunt impact of either 0 J, 0.6 J, or 1.2 J to the weight-bearing cartilage of the medial femur. The study was six months in duration. To evaluate the accuracy of MRI-derived measures of cartilage thickness, imaging acquired at time of euthanasia was compared to high-resolution contrast-enhanced micro-computed tomography (micro CT). 3-dimensional multimodal analysis demonstrated that morphometric MRI imaging is sensitive to sub-voxel changes in cartilage thickness. Therefore, MRI is a clinically relevant modality to quantify subtle cartilage damage, thereby presenting an opportunity to identify patients earlier in the disease process.

PUBLIC ABSTRACT

Osteoarthritis is a degenerative disease of the joints characterized by progressive loss of joint function, pain and disability. It affects most adults over fifty and is responsible for a significant proportion of direct and indirect costs of musculoskeletal disease. Due to the profound disability of late stage osteoarthritis, it is also associated with a host of comorbidities, including diabetes, heart disease, and obesity.

The hallmark of osteoarthritis is the onset of joint pain. Following a medical exam, a diagnosis of osteoarthritis is commonly confirmed by the presence of joint space narrowing on x-ray images. Unfortunately, diagnostics such as these are only sensitive to the latest stages of osteoarthritis, at which time irreversible damage has been done to the joint tissues, including cartilage and bone. Treatment of symptomatic osteoarthritis is currently limited to pain management and rehabilitation to reduce disability. When non-operative treatments are no longer efficacious, the damaged joint is commonly replaced with an artificial implant. These devices have achieved great success in enabling patients to return to their activities of daily living without debilitating pain.

Nevertheless, preservation of the native joint would be the preferred outcome and has been the primary aim of research efforts in recent years. Efforts have focused on two main areas: identification of the underlying mechanisms of osteoarthritis and development of diagnostics to screen for osteoarthritis in its earliest stages. Advances in either field offer the promise to inform new treatments that will forestall or outright prevent osteoarthritis. This work demonstrates the capacity of currently available clinical imaging to identify degenerative changes in cartilage morphology.

TABLE OF CONTENTS

LIST OF TABLES

LIST OF FIGURES

CHAPTER 1: INTRODUCTION

1.1 The burden of musculoskeletal disease

Musculoskeletal disease consists of a large group of chronic disorders affecting the structure and function of the muscles, tendons, ligaments, and bones of the human body. Common pathologies include low back pain, osteoporosis, and arthritis. The prevalence of musculoskeletal disease has been reported as high as 75% for individuals aged 65 and older. [1] This rate is 75% higher than the prevalence of cardiovascular disease and nearly 100% higher than the prevalence of chronic respiratory disease.

In 2011, the direct and indirect costs of musculoskeletal disease in the United States amounted to nearly $800 billion, a figure representative of approximately 6% of that year's gross domestic product. In 2012, 1 in 8 persons of working age reported lost work days due to a musculoskeletal condition. This equates to a staggering total of 216 million days of lost productivity. [2]

1.1.1 Osteoarthritis

Osteoarthritis (OA) is a musculoskeletal disease of the joints characterized by progressive articular cartilage softening, fibrillation, ulceration, and thinning; sclerosis and eburnation of subchondral bone; and the development of osteophytes and subchondral cysts (Figure 1-1). [3] OA may take years to develop and is commonly considered a disease of aging. Clinically, it presents with a variety of debilitating symptoms, most notably joint pain and stiffness. [4] Symptomatic OA is most commonly treated by joint arthroplasty.

OA is the most prevalent form of arthritis, affecting over 30 million Americans. From 2008-2011, annual medical expenditures for the treatment of OA amounted to nearly $340

billion. [5, 6] In addition, OA has been linked with increased rates of comorbidity, including heart disease, diabetes, and obesity [7, 8].

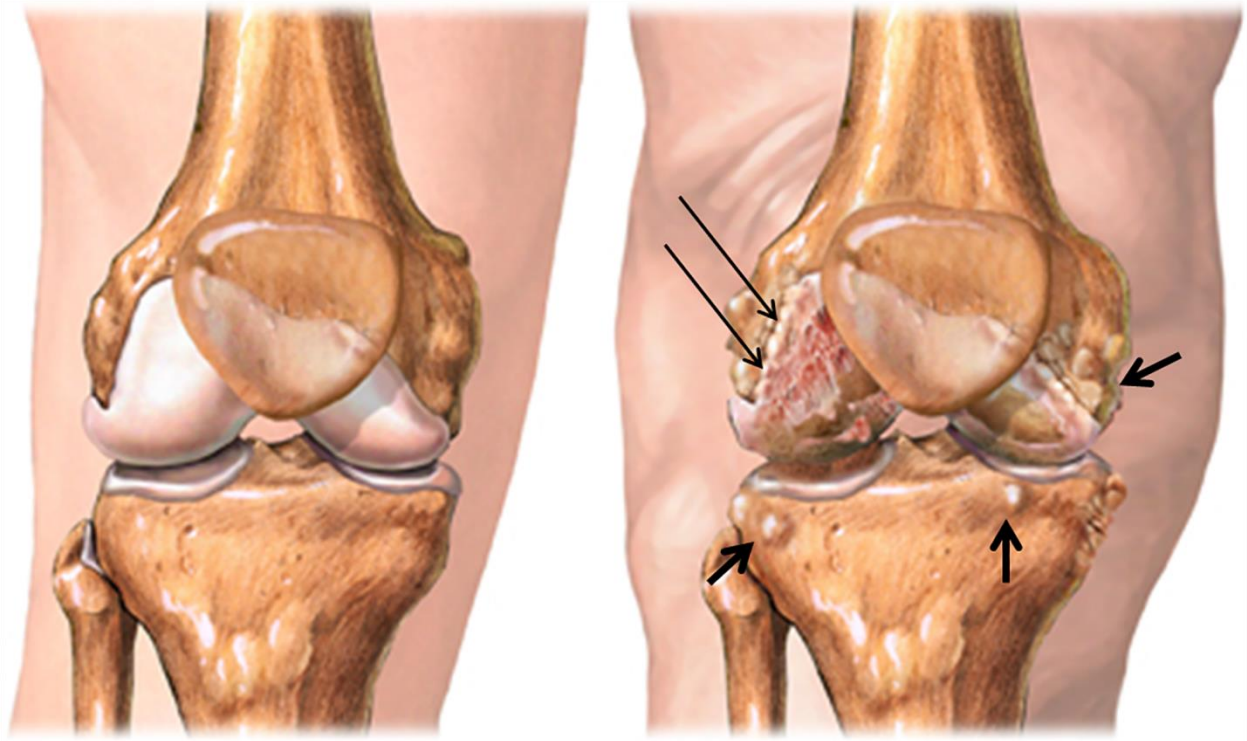

Figure 1-1 A healthy human knee (left) is compared to a severely osteoarthritic knee (right). The later stages of osteoarthritis feature deleterious morphological changes including articular cartilage loss (long arrows) and the development of bone spurs or osteophytes (short arrows). Break down of the cartilage surface leads to joint space narrowing, a hallmark feature of radiographic OA. [9]

1.1.2 Post-traumatic osteoarthritis

While chronic factors including aging, obesity, and genetics have been associated with the onset of OA, acute joint injury can also initiate the disease process. [10, 11] This secondary form of OA, or post-traumatic osteoarthritis (PTOA), affects 12% of the total number of Americans suffering from arthritis and accounts for healthcare costs of $3 billion annually. [11] PTOA tends to develop in younger, healthier, more active individuals than those typically suffering from OA, including athletes and members of the military. [8, 12, 13] In these groups, the incidence of PTOA as a proportion of OA has been documented as high as 28%, over twice that of the general population. [14] PTOA patients are likely to require arthroplasty nearly a

decade earlier in life than OA patients without a history of joint injury. [15, 16] In age-matched patients undergoing total knee arthroplasty (TKA) to treat OA, those with prior traumatic joint injury experience higher complication rates and less favorable functional outcomes than those without. [17, 18] This arises in large part from the fact that PTOA patients may present with certain artifacts of traumatic joint injury at the time of TKA, including scars, history of infection, malalignment, and stiffness. [19]

Post-traumatic osteoarthritis of the knee

The knee is one of the most frequently injured joints during sport and recreation [20, 21] and is also the joint most commonly affected by PTOA. [22] In the military literature, 100% of combat-related knee injuries result in an arthritis-related disability [14, 23, 24].

1.2 Motivations for studying PTOA

At the time of this writing, OA remains a treatable, but ultimately unpreventable disease. [25] Chronic and multi-factorial with late symptomatic presentation, the natural history of OA limits the acquisition of clinical data that might otherwise enhance our understanding of disease etiology. In order to evaluate the efficacy of novel therapeutic techniques, it is crucial that we develop methods of identifying features of joint injuries that will lead to osteoarthritis. In contrast to plain radiographs, these methods must be sensitive to the earliest features of disease. It is hoped that improved diagnostic techniques paired with a more complete understanding of the pathophysiology of OA will ultimately lead to preventative treatments.

PTOA provides a unique model in which the onset and progression of OA in humans may be studied. [26] In contrast to the factors associated with the onset of primary OA (e.g. age, genetics, body composition, health status), joint injury is a single initiating event that occurs at known time point, permitting longitudinal study. [12, 27, 28] The primary motivation of this

work was to develop a clinically relevant model of PTOA and evaluate the capability of diagnostic and morphometric clinical imaging to identify preclinical features of disease.

We hypothesized that PTOA following cartilage injury and joint overload would develop within 6 months and that the rate of onset would correlate with the severity of cartilage damage. This was studied in goat knees *in vivo*. PTOA progression was assessed by measuring time-dependent changes in the severity of acute cartilage injury.

This work set out to address the following questions:

(1) Is subtle cartilage thinning indicating early osteoarthritis present at time of sacrifice?

(2) Did more severe injuries lead to more rapid development of OA?

CHAPTER 2: LITERATURE REVIEW

2.1 Diagnosing osteoarthritis

Current clinical practice for establishing a diagnosis of OA tends to follow a general pattern. First, patients present with a variety of symptoms that commonly include joint pain, antalgic (limping) gait, crepitus (cracking noises during joint movements), reduced range of motion, swelling, and morning joint stiffness. [29] The incidence and relative severity of these symptoms are assessed through a combination of physical exam paired with a patient's medical history. Next, this information is collated, a list of possible causes is generated, and a physician narrows the list of possibilities through the process of differential diagnosis, ordering additional testing as needed to eliminate possibilities until a single hypothesis remains. A diagnosis of osteoarthritis is commonly verified by plain radiographs. If radiographic evidence is inconclusive, cross-sectional imaging including magnetic resonance imaging (MRI) and multi-detector computed tomography (MDCT) may be performed.

Radiographs offer a fast and relatively low cost method of non-invasively visualizing joints. They are the most widely used imaging modality for diagnosing OA. Radiographs are commonly used to assess a variety of osteoarthritic joints, including the knees, hips, spine, and other sites in the upper and lower extremities. Standardized imaging planes have been established for imaging each joint. In the knees, the clinical standard for OA assessment is a standing anteroposterior (AP) radiograph. Features of interest include joint space narrowing (Figure 2-1), sclerosis of the subchondral bone, and evidence of osteophytes. [30] The relative severity of these features may be quantified using semi-quantitative scoring systems. Semi-quantitative scoring of plain radiographs is a mainstay for risk stratification in clinical and epidemiologic studies of OA. [31]

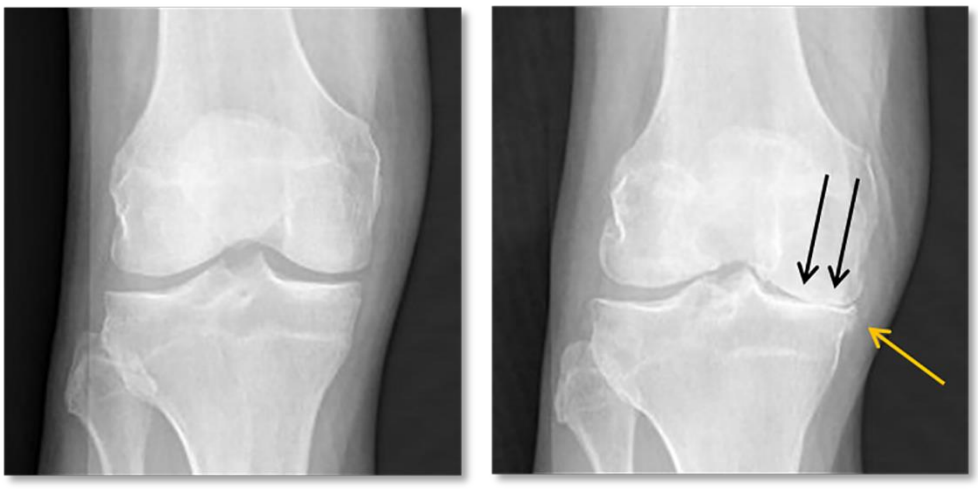

Figure 2-1 Plain radiographs are the clinical gold standard of confirming a diagnosis of osteoarthritis. For knee OA, a standing AP radiograph is typically ordered. A healthy knee is shown on the left. Note the space between opposing femoral and tibial surfaces in the medial and lateral compartments. An osteoarthritic knee is shown on the right. In contrast to the healthy knee, this joint space shows evidence of joint space narrowing (black arrows) and osteophyte development (orange arrow).

Ultimately, the features that clinical assessment and plain radiographs screen for are characteristics of end stage OA. Treatments to preserve the native joint are limited at this advanced stage; care essentially comprises symptom management until eventual joint replacement. Although joint arthroplasty is an established method of improving joint function and reducing pain, the gold standard of treatment is the native, healthy joint. Earlier diagnostics offer the opportunity to identify OA patients before irreversible joint change and administer treatments to preserve the native joint. A variety of tools offer the opportunity to accomplish this.

2.1.1 Non-imaging diagnostics

In many cases, joint pain precedes joint space narrowing. Therefore, stratifying levels of patient pain may be an effective method of identifying early arthritic change. Scoring systems such as the visual analog scale and numeric rating scale offer a means of accomplishing this. [32] Pain-based functional indices include the Lysholm Knee Scoring Scale [33], WOMAC [34], Knee Injury and Osteoarthritis Outcome Score (KOOS) [35] have also been studied at length.

Pain scoring systems offer clinicians a simple, inexpensive assessment to aid in differential diagnosis.

Abnormal biomechanics have a well-established contributing role in the onset and progression of OA. Therefore, non-imaging morphological and movement parameters may also be predicative of the early stages of disease. Most notably, gait analysis is not predicative of the early stages of osteoarthritis. [36] Malalignments of the lower extremity, including knee varus and valgus have also been examined. Of these two, varus has been associated with an increased risk of tibiofemoral OA. [37] Leg length discrepancies have been associated with osteoarthritis of the knee [38] and hip [39-41].

2.1.2 Cross-sectional Imaging

Non-imaging diagnostic tools are an important part of pre-radiographic osteoarthritis assessment. However, the greatest opportunities for early diagnosis lie in cross-sectional imaging. By enabling visualization of morphometric or compositional joint features in three dimensions, these techniques enable direct joint measurements.

Computed tomography

Multi-detector computed tomography (MDCT) is a non-invasive cross-sectional clinical imaging modality that provides excellent visualization of bone. In OA research, MDCT has been used to study the development of subchondral cysts and sclerosis, trabecular remodeling, and bone density changes. MDCT is an x-ray based method of constructing a 3D volume, relying on the composite volumetric information by capturing a series of radiographic projections at small degree increments while rotating 180 or 360 degrees around a stationary subject. Consequently, MDCT has a number of shortcomings similar to plain radiographs, including radiation exposure and the inability to resolve soft tissues, that limit its utility for early-stage OA diagnosis.

Micro computed tomography (micro CT) is a variant of CT imaging capable of resolving structures at a micrometer level. As a small animal or *ex vivo* research imaging modality, micro CT has provided tremendous insights into changes in bone microarchitecture associated with the onset of OA. [42, 43] In spite of similar shortcomings to MDCT, introduction of a radiopaque contrast medium prior to scanning has turned micro CT scanning into an effective technique for visualizing cartilage morphology and composition, and it has become an indispensable tool for *in situ* and *ex vivo* studies. [44, 45] While this technique has largely remained a tool of research, *in vivo* investigations are currently underway with the ultimate aim of providing earlier clinical diagnostics of joint health and disease risk.

Magnetic resonance imaging (MRI)

MRI is a non-invasive cross-sectional method of visualizing a variety of joint soft tissues including cartilage, meniscus, bone marrow, synovium, capsule, and ligaments. It is the most common imaging modality employed in osteoarthritis research and has a documented history of identifying pre-clinical joint abnormalities. [46] MRI features no ionizing radiation and can in some cases be performed in weight bearing postures. [47] Although cost and availability of scanners have thus far prevented MRI from becoming the new clinical norm of diagnostic screening for OA, MRI-derived imaging biomarkers of cartilage thickness and volume have been evaluated in recent clinical trials. [48, 49]

The idea at the core of MRI is that protons aligned in a strong magnetic field will realign with the field at a measurable rate when perturbed and that this rate will serve to distinguish different tissues. A variety of imaging sequences - which may be broadly thought of as different methods of proton perturbation - have been developed to provide complementary morphologic and compositional information about joint tissues. Common sequences for visualizing cartilage

include T1 and T2-weighted and, double echo steady state (DESS) and T1ρ imaging provide crucial morphologic and compositional information, respectively.

2.1.3 Imaging-based assessment

Imaging-based assessment of OA falls under three distinct categories. The first, subjective assessment, consists of an expert interpretation of medical imaging data to identify features of disease. The second, semi-quantitative assessment, occurs when an expert identifies and grades the severity of specific disease-relevant features using a list of standardized criteria. In MRI, semi-quantitative assessments such as the whole organ magnetic resonance imaging score (WORMS) have played an important role in clinical studies of OA. [50, 51] The third category, quantitative analysis, relies on the direct measurement of imaging features to describe disease. Although all three categories of assessment require a combination of pattern recognition and rule-based heuristics to provide valid diagnostics, quantitative analysis offers the most potential to identify the underlying mechanisms of disease and inform efforts to develop preventative treatments. Quantitative analysis will be the main focus of this work.

For any quantitative biomarker to be valid, it is imperative that it meet a number of criteria. First, it must be reproducible. Specifically, this means that the value of a measure will not change for repeated measurements of the same data. For example, cartilage volume measurements rely of the extraction (segmentation) of cartilage features. Consistent segmentation procedures are required compare volume measures or calculate statistics. [52-54] In addition, medical imaging based measures must be accurate, specific, sensitive to longitudinal change, and acceptable to regulatory agencies. [55] Clinical morphometric and diagnostic MRI sequences offer considerable information from which to extract quantitative measures and the benefit of immediate implementation into a clinical population. Therefore, in lieu of novel imaging techniques which may be years away from clinical use, these sequences offer the best

opportunity to study disease pathophysiology and identify patients at greatest risk of developing OA.

2.2 Treating OA

Current treatments are unable to prevent or reverse OA. [10, 11, 22, 56] However, a variety of options are available for managing symptoms and improving function prior to joint replacement. These interventions encompass the following categories: nonpharmacologic, pharmacologic, complementary and alternative, and surgical. [57]

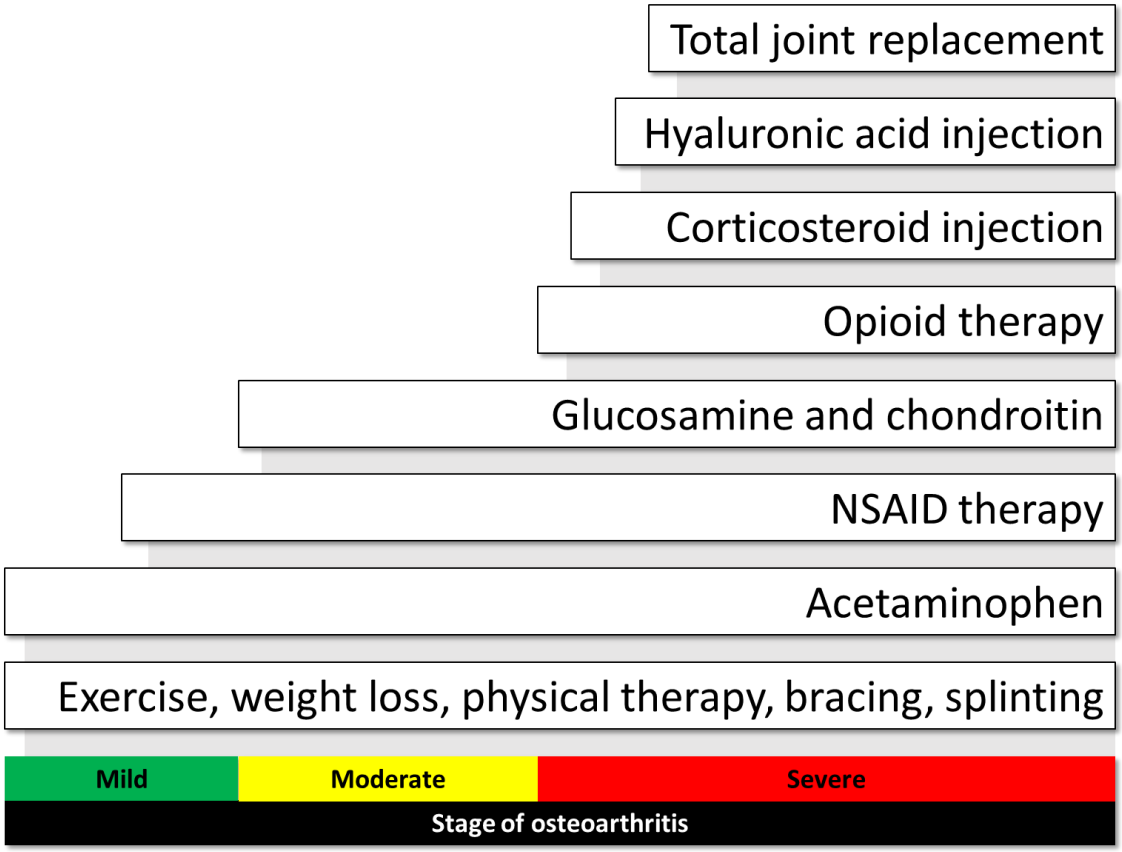

Figure 2-2 Clinical care follows a stepped approach according to the stage of osteoarthritis a given patient is in. Mild treatments include exercise, weight reduction, and pharmacologic interventions to treat pain and improve range of motion. As the disease becomes more advanced, more aggressive pharmacologic treatments may be prescribed. Joint replacement is considered when these treatments prove ineffective to mediate disease symptoms. This stepped care approach has been adapted from the American and British guidelines for clinical care of osteoarthritis. [58, 59]

Non-pharmacologic interventions include exercise, ultrasound therapy, weight reduction, and bracing or the use of other assistive devices (i.e. canes). Nonpharmacologic is the first line of defense against mild OA and can be continued as a therapeutic through end stage OA. Although alternative treatments such as acupuncture have been proven ineffective and the efficacy of topical analgesics invites debate, there is a small body of evidence to support the use of glucosamine and chondroitin to treat moderate to severe knee OA.

Pharmacologic treatments represent the second tier of OA treatment. Common pharmacologic agents utilized include non-steroidal anti-inflammatory drugs (NSAIDs) and acetaminophen. Current pharmacologic treatment seeks to provide relief from symptoms. Opioids may be employed as a follow-up option if acetaminophen or NSAIDs prove insufficient to reduce pain. Corticosteroid or hyaluronic acid injections may be warranted for cases of severe OA.

The definitive treatment available to manage OA is surgery. This level of intervention is acceptable when more conservative treatments are ineffective. The outcomes of partial or full joint replacement have been investigated and it is well established that these procedures successfully reduce pain and improve function. Unfortunately, this intervention fundamentally fails to treat the underlying causes of osteoarthritic change.

2.3 Modeling OA

Due to its chronic and multi-factorial onset, modelling OA to learn more about its underlying pathophysiology has proven to be a formidable challenge. The acute and immediate implications of traumatic joint injury have provided a platform from which models of PTOA may be established. It is generally accepted that conclusions about the underlying features of

PTOA onset and progression enhance our understanding of OA to ultimately develop more effective screening methods and treatments.

Models offer the opportunity to isolate specific, clinically relevant features of trauma that have been associated with disease onset and progression. Anterior cruciate ligament (ACL) rupture is one of the most common injuries implicated in the onset of PTOA. [60-64] During an ACL rupture, the posterior tibial plateau is driven into the femur, resulting in a blunt impact injury to the joint surface. Blunt mechanisms are a common contributor to joint injuries, playing a role in 90% of all non-military joint trauma. [65-67] About half of all ACL rupture patients will develop PTOA within 10-20 years of injury. [12, 28, 62] Secondary knee pathology including meniscal tears and chondral lesions have been associated with ACL rupture injuries. [60, 68]

Meniscal injury has been associated with the onset of PTOA in as many as 50% of patients 10-20 years after the initial traumatic event. [61, 69] Loss of an intact meniscus can cause widespread overload of the weight-bearing articular cartilage. [70] In an effort to protect the cartilage and reduce pain, arthroscopic procedures to repair the meniscus or partial meniscectomy are commonly performed. Despite the therapeutic intent of partial or full meniscectomy, both procedures are responsible for abnormal changes in joint loading associated with the onset of OA. [70-73] Meniscal tears occurring secondary to ACL rupture are significantly more likely to occur in the medial compartment. [74]

In a retrospective study of over twenty-five thousand knee arthroscopies of cartilage injury, 70% of chondral lesions were associated with non-cartilage injuries. The most common secondary feature was meniscal injury (37%). [75, 76] Lesions to the articular cartilage may be partial or full thickness and include the subchondral bone. Cartilage lesions in the knee are commonly found in the medial femoral compartment. [75-78] The presence of tibiofemoral

cartilage defects has been identified as a risk factor of PTOA, even in the absence of radiographic evidence. [79] Owing to the limited healing capacity of articular cartilage, the repair of chondral lesions is an important priority in orthopaedic management of PTOA.

Once appropriate features have been identified, it is crucial to select a research vehicle in which to model these features. Translational research commonly uses animal models in which PTOA is specifically created. Genetic and phenotypic features may be controlled to limit biological variability, and the effect of injury may be assessed longitudinally, with the benefit of pre-injury assessment and end stage histologic analysis. In contrast to clinical research, which may only identify associations between disease and features predicative of it, translational research permits one to draw mechanistic conclusions based on empirical evidence. [80-82]

Notably, there is no standard animal model to facilitate the study of PTOA, owing to the variety of underlying pathologies that might be investigated. Therefore, a variety of animals have proven effective to the modeling and study of PTOA. These include mice, rats, rabbits, guinea pigs, dogs, sheep, goats, and horses. [83]

Small animals (mice, rats, rabbits, and guinea pigs) are primarily used for investigating specific mechanisms of disease or preliminary studies assessing the effectiveness of novel therapeutics. This is due to certain features of small animal research, including lower costs and more genetic control (e.g. knockout mice). In contrast, large animals (dogs, pigs, sheep, goats, and horses) provide more clinically relevant data and are required as part of the process to introduce a new diagnostic or treatment into a clinical setting. Compared to small animals, large animals have more human-equivalent anatomy and biomechanics, may undergo routine diagnostic imaging or arthroscopy, and can serve as a model for evaluating post-operative

management such as joint distraction. [84] Since the primary objective of this work was to evaluate the diagnostic potential of clinical imaging modalities, a large animal was preferred.

A number of features make sheep or goat PTOA models more appealing for studying meniscal injury and chondral lesions of the knee than other large animals. First, their knees are grossly similar in anatomy to human knees. [84-86] This enables the implementation of clinically relevant diagnostic imaging procedures. Second, and in contrast to dogs, goats and sheep do not rapidly develop PTOA when the anterior cruciate ligament is transected. [87] Instead, goat or sheep models of PTOA frequently feature full or partial meniscectomy. [73, 88-90] Although goat and sheep stifles (knees) are similar to each other both biomechanically and anatomically - including the presence of a digital extensor tendon that crosses anteriorly in the lateral compartment – articular cartilage is thicker in goats than in sheep. Thus, goats offer more human-equivalent cartilage thickness and were selected for use in this work.

CHAPTER 3: MODELING LOCAL AND WHOLE JOINT CARTILAGE CHANGES IN A LARGE ANIMAL

This chapter discusses the development and implementation of methods to induce cartilage injury for subsequent study using MR imaging. Specific injury characteristics included a focal joint defect and more subtle whole-joint load changes associated with changes in mechanical loading. The creation and mechanical characterization of these injuries were studied *ex vivo* before being implemented in a common orthopaedic large animal model (goat). The choice of the goat was primarily that it was deemed the best species in which to use MR imaging given that goats stifles feature human equivalent cartilage thickness, joint size, and gross anatomical features. Therefore, they are desirable for the translational study of the local and whole joint changes that precede the onset of osteoarthritis.

3.1 Development and testing of surgical methods

The amount of energy imparted by blunt impact trauma on articular cartilage has been identified as a risk factor of PTOA onset. [91] To investigate the capability of clinical MR imaging to differentiate between levels of injury severity and screen for patients at higher risk of disease, it was necessary that we develop a repeatable method of creating cartilage blunt impact injuries. Specifically, we needed a device with the capacity to modulate impact energy and which could be sterilized and positioned normal to the weight bearing articular cartilage in the knee. Many examples of cartilage impact devices have been documented in the literature. Drop towers [92], spring loaded devices [93], and pendulums [94] included some, but not all, of our design criteria. Therefore, we developed our own impact device by creating a gauge related pneumatic impact gun by adapting a commercially available pneumatic stapler (SureBonder Model 9600, Wauconda, IL).

In conventional use, this stapler relies on an air pressure pulse to accelerate a ram that in turn drives a common staple. We modified it to drive a 35-mm long nonporous stainless steel rod with a diameter of 6 mm (Figure 3-1). Previous work has shown this diameter impact face to be sufficiently large to prevent rim stress concentrations and shearing of the cartilage from the subchondral bone during impact [95, 96]. To ensure that contact pressure at the gun-cartilage interface is consistent prior to impact delivery, the trigger will not engage until resistance from a spring-loaded pin at the rod-gun interface has been overcome (Figure 3-1a). A 1-mm long, 30-degree conical spike machined into the impact rod face (Figure 3-1b) prevents the impact face from slipping along the cartilage surface. When the trigger is pulled, the impact face is driven against the cartilage surface by an air pressure pulse.

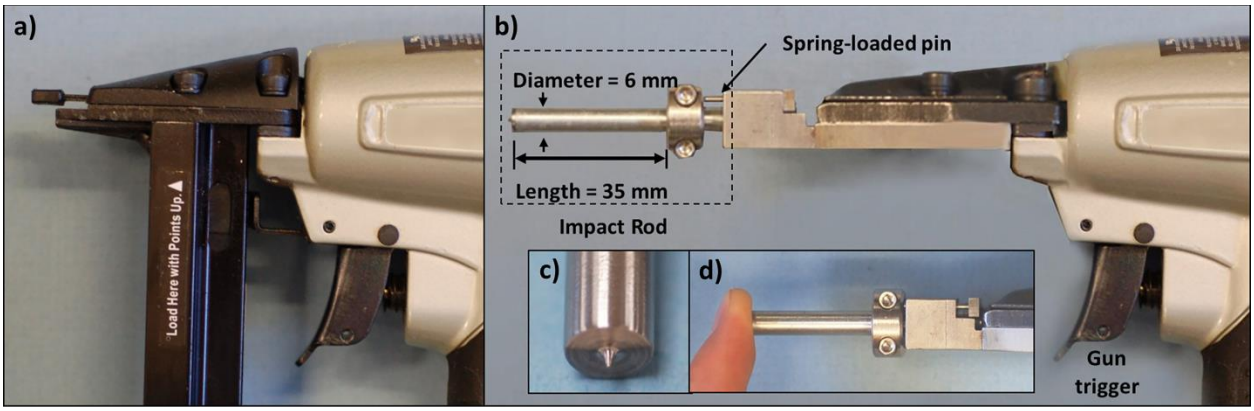

Figure 3-1 The development of the cartilage impact gun. (panel a) This is the unmodified pneumatic stapler. In conventional use, an air pressure pulse is used to accelerate the ram (at top left) and drive a commercial staple. (panel b) The cartilage impact gun featuring a custom-machined, 6-mm diameter, stainless steel impact rod (dashed box). (panel c) A 30-degree 1-mm long conical spike has been machined into the impact rod face to prevent slippage when the rod is brought into contact with cartilage. (panel d) The trigger is engaged when the impact rod has been fully compressed.

3.1.1 Creating a blunt impact injury: foam specimen validation study

Although a pneumatic stapler confers the ability to modulate impact energy by design, this feature is of little use in a research without proper calibration. Calibration permits the correlation of gauge pressure with impact energy, enabling direct comparisons between energy

and time to disease onset. This also provides the opportunity to compare outcomes with other models described in the literature.

Device calibration was accomplished through benchtop tests using rigid polyurethane foam blocks (density = 0.32 g/cm^3). In material testing applications, this density is more commonly associated with trabecular bone. [97] However, an optimal material for device calibration need not necessarily be representative of its intended application. Rather, an optimal medium is one which is homogenous and deforms in a reproducible, measurable way. The foam blocks utilized for testing met these criteria. Were the gun's effect on cartilage the primary aim, cartilage explants would have been the preferred material.

During the first calibration test, seven replicate impacts at air pressures of 30, 40, 50, and 60 pounds per square inch (psi) were delivered to the foam blocks using the impact gun. These pressures were selected in order to test over a range which would yield a linear stress-strain relationship and generally approximate physiologically relevant impact energy. Notably, the recommended operating pressure of the gun is actually 60-100 psi. A digital caliper was used to measure the indentation depth of each trial. Mean indentation depth was calculated for each air pressure. A linear equation was fit to the plot of mean impact depth vs. applied air pressure. (Figure 3-2) This relationship is expressed in Equation 3-1. The impaction gun was able to deliver repeatable, well controlled impacts as indicated by small standard deviations in the penetration depths obtained during testing using the polyurethane foam (Figure 3-2, lower left) and excellent correlation ($R^2 = 0.99$) between impact depth and air pressure.

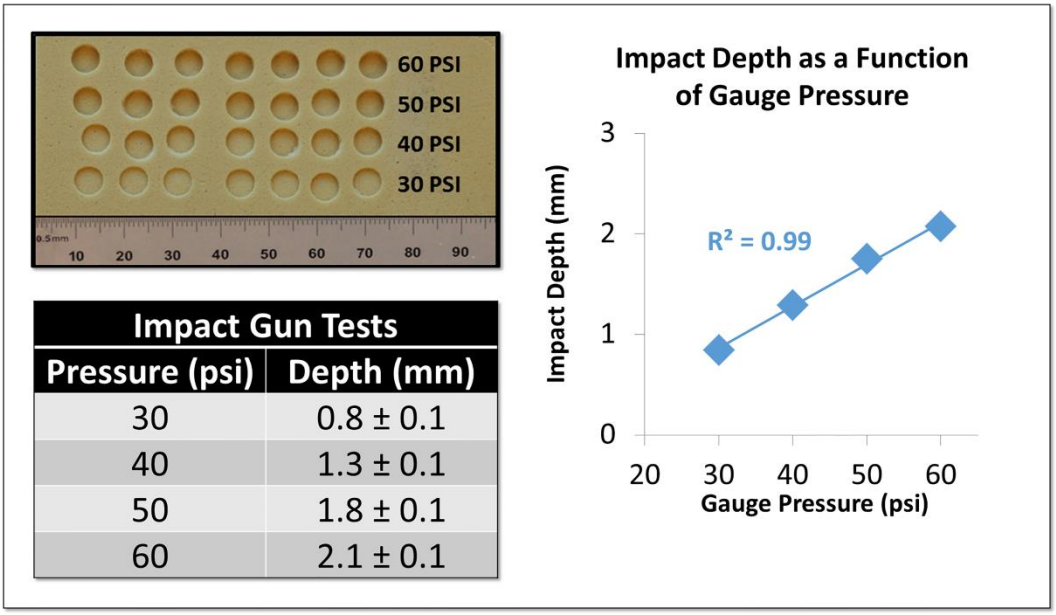

Impact Gun Tests	
Pressure (psi)	Depth (mm)
30	0.8 ± 0.1
40	1.3 ± 0.1
50	1.8 ± 0.1
60	2.1 ± 0.1

Figure 3-2 Polyurethane foam block testing. The impact gun was used to create seven replicate impacts at pressures of 30, 40, 50, and 60 pounds per square inch (psi) (top left). These levels were selected to fall within the linear region of the stress-strain curve for the foam material. Impact depth was measured for each level with a micrometer (bottom left). Mean depth was plotted versus pressure (right). Note that there is a nearly perfect linear correlation (R^2 value). Linear regression curve fitting was performed to derive a numerical relationship between gun pressure and impact depth. The equation of this line is reported in Equation 3-1.

$$\boldsymbol{Impact\ Depth = 0.0415 * Gauge\ Pressure - 0.38}$$

Equation 3-1 Depth vs. Pressure regression equation

In the second calibration test, an MTS 810 servohydraulic material testing system (MTS Systems Corporation, Eden Prairie, MN) was used to drive the impact rod to depths of 1.0, 1.5, 2.0, and 2.5 mm under displacement control (four trials of each depth, 0.1 seconds per trial; Figure 3-4). An axial load cell measured force during each trial. Using this real-time data, plots of force versus impact rod displacement were generated (Figure 3-3). Each curve was integrated to calculate impact energy (Equation 3-2). Linear regression was performed on the plot of impact energy and depth, establishing a numerical relationship between the two (Figure 3-4, Equation 3-3).

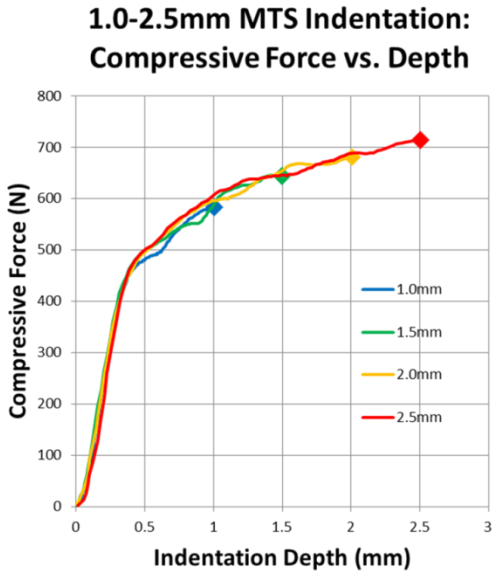

Figure 3-3 Using the data recorded during impact testing with the MTS, instantaneous compressive force has been plotted versus impact rod displacement. The integral of each curve corresponds to the energy of impact. From this data, impact energy was calculated and plotted versus impact depth.

$$Energy\ (Joules) = \int_0^{x_{max}} Fdx \approx \Sigma F \Delta x$$

Equation 3-2 Formula to calculate impact energy from MTS force-depth data

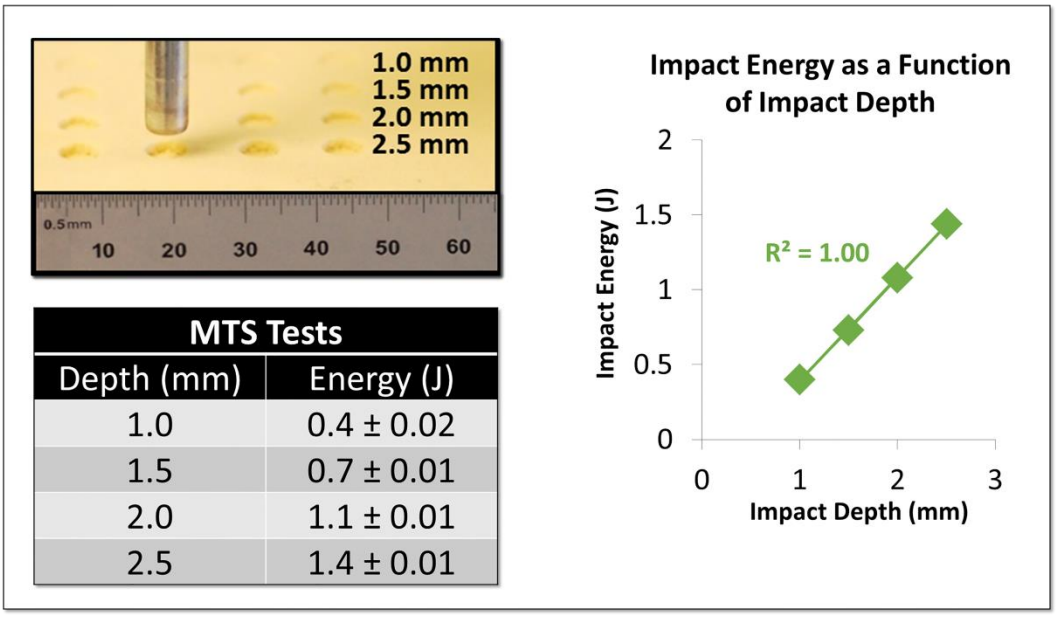

MTS Tests	
Depth (mm)	Energy (J)
1.0	0.4 ± 0.02
1.5	0.7 ± 0.01
2.0	1.1 ± 0.01
2.5	1.4 ± 0.01

Figure 3-4 Polyurethane foam block testing. A materials testing system (MTS) was used to drive the impact rod to depths of 1, 1.5, 2, and 2.5-mm at a rate of 0.1 seconds per trial. Four replicate trials were performed for each depth (top left). Impact energy was calculated for each depth by calculating the work performed during each test (Figure 3-3, Equation 3-2; reported in bottom left). Impact energy was plotted versus impact depth (right). Note that there is a nearly perfect linear correlation (R^2 value). Linear regression curve fitting was performed to derive a numerical relationship between impact energy and impact depth. The equation of this line is reported in Equation 3-3.

$$Energy = 0.694 * Impact\ Depth - 0.302$$
Equation 3-3 Depth vs. energy regression equation

To describe impact energy (J) as a function of impact gun air pressure (psi), the impact depth vs. air pressure equation was substituted into the impact energy vs. impact depth equation (Equation 3-4). Establishing a quantitative relationship between gun pressure and energy is critical to characterizing injury severity and its role in the development of PTOA.

$$Energy = 0.0288 * AirPressure - 0.566$$
Equation 3-4 Equation of energy and air pressure

In contrast to other types of blunt impact devices, the impact gun is a portable and maneuverable hand-held instrument. Although other examples of handheld, spring-loaded cartilage impact devices are present in the literature [93, 95], our pneumatic device presents a novel approach with a number of critical advantages. First, minimal recoil during impact ensures that the gun is held steady and that energy is delivered to the tissue and not dissipated by the device itself. Second, injury severity is simply and reliably modulated by gauge pressure. Both features ensured the resultant focal defects were highly consistent. The rigid foam used to calibrate the impact gun was not representative of its intended use on cartilage, rather it was specifically chosen for its homogenous material properties. This ensured that impact reproducibility could be evaluated independently of inter-specimen variability prior to using the device on cartilage.

3.1.2 Quantifying changes after partial meniscectomy and blunt impact injury

Following gun calibration, we needed to evaluate the changes in joint contact stress following partial meniscectomy and focal blunt impact to the weight bearing articular cartilage. For this study, the knees of nine skeletally mature sheep (mean mass 92 kg) euthanized for other IACUC-approved studies at our institution were harvested and frozen for subsequent mechanical measurement. Sheep feature knees that are anatomically and biomechanically equivalent to

goats. [84] Taking these similarities in account, as well as the availability of freshly harvested sheep knees from a concurrent research project at our Institution, we elected use sheep as a stand-in for goats in this work.

Prior to testing, each specimen was thawed for 24 hours at room temperature and dissected free of overlying muscles and other soft tissues while leaving the joint capsules intact. The proximal femur and distal tibial shafts were potted in polymethylmethacrylate (PMMA) to maintain the joint at 60 degrees of knee flexion, the angle at which peak loading occurs in the sheep gait cycle [98].

Immediately prior to testing, the joint capsule was incised both anteriorly and posteriorly and a calibrated contact pressure sensor (a bisected Tekscan model 5033, South Boston, MA with a resolution of 72 sensels per square centimeter) was inserted into the medial and lateral compartments of the knee, proximal to the menisci (Figure 3-6a) [72, 99, 100]. To prevent sensor shifting during testing, the free ends of the sensor were secured to the posterior proximal femur with screws. The joints were then set one at a time in a custom axial loading fixture mounted into an MTS 810 system (Figure 3-5). This fixture employed a low-friction sled to allow for knee adduction and abduction. The loading fixture permitted knee varus/valgus and internal/external rotation of the tibia but was otherwise constrained.

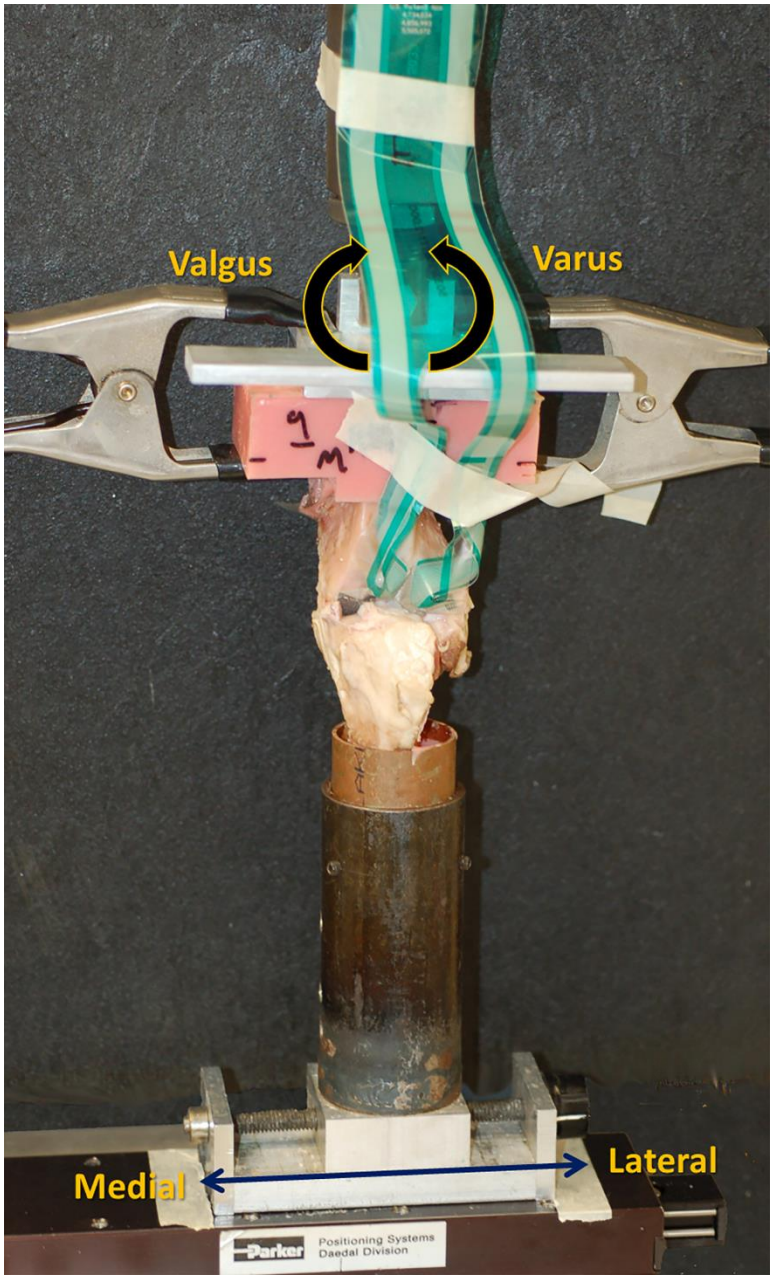

Figure 3-5 The testing apparatus used to measure knee contact stress. Dissected knee joints were potted in PMMA proximal and distal to the joint at 60 degrees knee flexion. A bisected Tekscan ankle sensor was inserted into the medial and lateral compartments between the menisci and femoral condyles. The proximal segment was mounted into an MTS with a hinged fixture permitting rotation about the anterior-posterior axis (varus/valgus rotation). The distal segment was mounted into a fixture on a frictionless sled, permitting medial-lateral translation under loading conditions. Pressure maps were recorded for the intact knee, post-meniscectomized knee, and post-meniscectomized knee with blunt impact trauma to the weight bearing cartilage. The specimen pictured above has undergone partial meniscectomy.

To simulate peak load during normal sheep gait, a ramp load of 900 N (equivalent to twice the average sheep body weight [98]) was applied at a rate of 100 N per second. With the

900-N load applied, the Tekscan sensor recorded baseline intact knee contact pressure simultaneously in the medial and lateral compartments (Figure 3-6b). To alter joint loading via partial meniscectomy, the 900-N load was removed and a 5-mm wedge was excised from the anterior horn of the medial meniscus, taking care to preserve the adjacent cartilage and sensor (Figure 3-6a). The 900-N load was then reapplied and a second Tekscan recording was taken (Figure 3-6b).

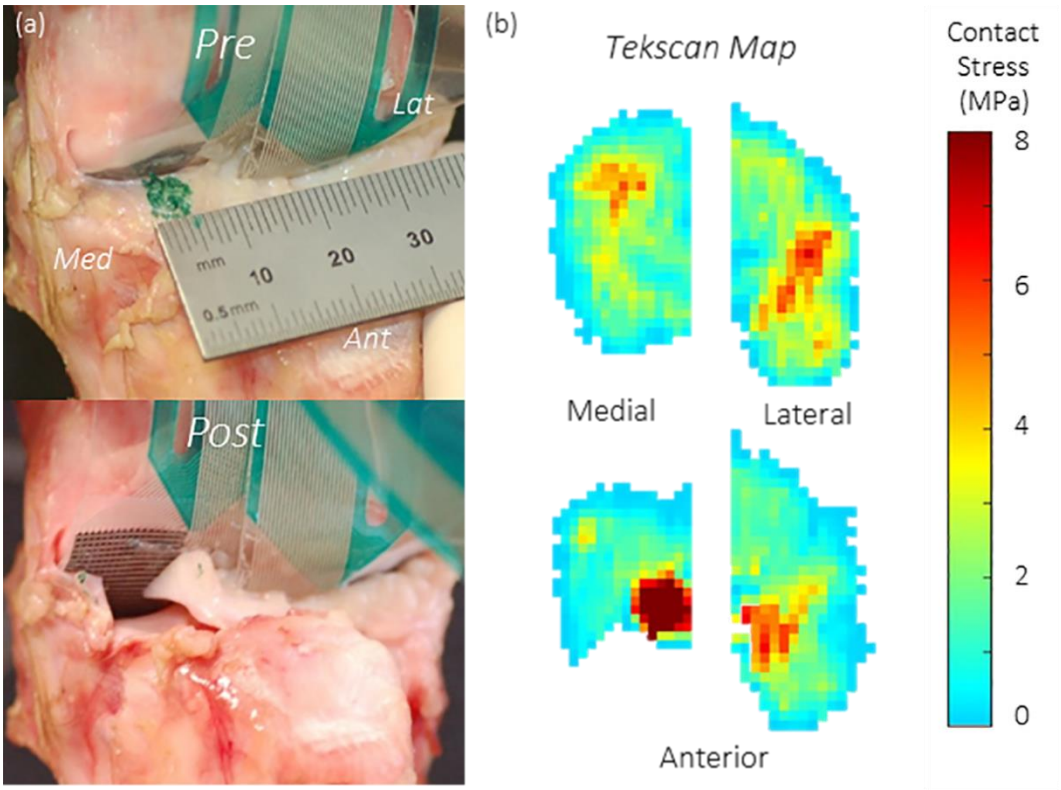

Figure 3-6 (a) The left-hand column depicts the partial meniscectomy procedure developed in this work. A 5-mm wedge of the anterior horn (upper left panel, marked in green) is excised from the anterior horn of the medial meniscus (lower left panel). (b) The right-hand column depicts the contact stress, as measured with Tekscan. Note that there is a sharp increase in peak contact pressure and decrease in contact area in the medial compartment of the meniscectomized knee. The lateral compartment is not significantly affected by this procedure.

Approximately twelve months after the initial contact stress testing to evaluate the effect of partial meniscectomy on joint loading, a follow-up series of tests were performed to examine the effect of blunt impact on contact. Based on the findings of previous work in which the biomechanical effect of rim stress concentration was found to be insignificant for defects of 10-

mm or less in diameter, our preliminary investigation had assumed that blunt impact trauma did not appreciably change contact pressure. [101] However, this premise was revisited following receipt of a critique that an investigation into the combined effects of partial meniscectomy and impact were warranted.

First, specimens underwent the preliminary loading, partial meniscectomy, and follow-up loading to characterize the effect of partial meniscectomy in isolation. Next, the specimen and loading fixture were removed from the MTS for creation of a focal cartilage lesion. Taking care to prevent movement of the Tekscan sensor, the specimen was flexed to 100 degrees to expose the weight-bearing cartilage surface of the medial femoral condyle. The impact gun was manually positioned normal to the articular cartilage surface and a 1.2 J impact was delivered. The knee was then extended to its original position and replaced in the MTS, and a final cycle of loading and contact pressure recording occurred.

At the time that this experimental step was added, three of the original five specimens had been harvested for use in another project and were therefore not available for further testing. The two remaining specimens (specimens 2 & 3) - which had been frozen- were included in the follow-up testing with four new specimens, following verification that the contact stress profiles were consistent with the pattern of stress observed previously in the partially meniscectomized state. Despite these similarities, the peak stress, contact area, and center of pressure measures had shifted from the original testing. Therefore, the original tests with these specimens were denoted 2a/3a and the follow-up tests were denoted 2b/3b.

Raw Tekscan data and sensor calibration curves were loaded into a custom MATLAB (The Mathworks, Natick, MA) program for analysis. First, the algorithm filled used linear interpolation to fill in every other row. This was a necessary procedure because every other row

was lost when the Tekscan sensor was bisected in order to cover both compartments. Second, East-West and North-South linear interpolation was performed to account for any additional rows or columns which may have dropped out due to the strain required to maneuver the sensors into position and accommodate joint tissue geometries. Next, stress maps were visually inspected to confirm that the site of peak loading was not located near the edge of the contact patch, a condition which would have suggested that the point of peak loading had not been captured by the sensor. This was not a feature of any maps. Peak contact stress, contact area, total load recovery, and center of pressure (CoP) were calculated for the medial and lateral compartments in the intact, overloaded, and impact conditions. A composite image illustrating the changes in contact stress before and after partial meniscectomy is depicted in Figure 3-7.

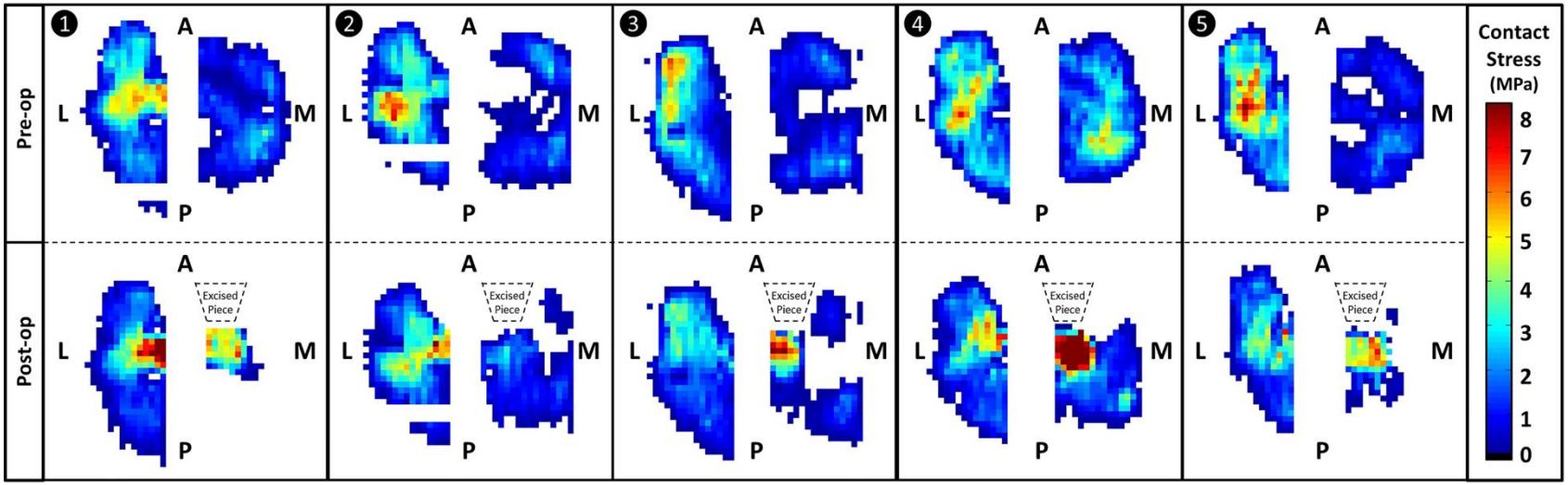

Figure 3-7 An illustration of the changes in contact stress that follow partial meniscectomy for a representative sample of five sheep knees. Each panel contains a map of the lateral and medial compartments (L = lateral, M = medial, A = anterior, P = posterior). The top row is the pre-operative state. Contact stress in the post-meniscectomized knee is depicted in the bottom row. A dotted region corresponding to the approximate location of excised meniscus has been provided in each of the lower panels. Note that there is a distinctive reduction in contact area and increase in contact stress in the medial compartment. Contact pressure is depicted in mega-pascals (MPa).

3.1.3 Results

Statistically significant increases in peak contact stress (~171% increase; p=0.03) and decreases in contact area (~35% decrease; p=0.001) were observed in the medial compartment after partial meniscectomy (Table 3-1). These results are consistent with the work of Lewinski et al., in which peak contact stress increased by an average of 260.4% and contact area was reduced by 55% compared to controls in a study of fully meniscectomized sheep knees. [72]

Table 3-1 Average (±1 standard deviation) measurements of peak stress, contact area, and center of pressure (CoP) shift in each compartment

Compartment	Measure	Pre-op	Post-apm$^{\gamma}$	P-value (vs pre-op)*	Post-impact	P-value (vs post-apm$^{\gamma}$)*
Medial	Peak Stress (MPa)	4.9 ± 2.4	8.4 ± 3.4	0.03	10 ± 5.4	0.5
	Contact Area (mm^2)	252 ± 32.5	163 ± 66.5	0.001	156 ± 57.2	0.9
	AP CoP Shift (mm)$^{\delta}$		-0.52 ± 1.5	0.7	-0.45 ± 1.3	0.8
	Cruciate/Collateral CoP Shift (mm)$^{+}$		2.6 ± 0.89	0.0040	-0.19 ± 0.43	0.8
Lateral	Peak Stress (MPa)	6.8 ± 1.7	7.7 ± 2.7	0.5	6.3 ± 2.9	0.4
	Contact Area (mm^2)	240 ± 24.1	226 ± 21.5	0.1	212 ± 32.3	0.5
	AP CoP Shift (mm)$^{\delta}$		-0.24 ± 0.37	0.9	0.066 ± 0.39	1.0
	Cruciate/Collateral CoP Shift (mm)$^{+}$		1.2 ± 0.68	0.03	0.036 ± 0.58	1.0

δ positive indicates a posterior CoP shift, negative indicates an anterior CoP shift
+positive indicates a CoP shift towards the cruciate ligaments; negative indicates a CoP shift towards the collateral ligaments
*CoP shift p-values calculated from position, not shift
$^{\gamma}$ apm = anterior partial meniscectomy

Although the shift in the location of the CoP in the anteroposterior direction failed to achieve statistical significance (medial compartment: -0.52 ± 1.5 mm, p = 0.7; lateral compartment: -0.24 ± 0.37, p = 0.9), there was a significant shift of the CoP towards the middle of the joint in both compartments after partial meniscectomy (medial compartment: 2.6 ± 0.89, p = 0.004; lateral compartment: 1.2 ± 0.68, p = 0.03). Stress, contact area, and CoP measurements for each specimen are presented in following tables: Table 3-2, Table 3-3, and Table 3-4.

Table 3-2 Peak stress, all specimens

Specimen Number	Peak Stress (MPa)					
	Medial Compartment			Lateral Compartment		
	Pre-op	Post-apm	Post-impact	Pre-op	Post-apm	Post-impact
1	3.9	6.6		6.0	9.7	
2a	3.3	3.2		7.1	8.8	
2b		6.2	4.4		12.0	9.5
3a	2.9	9.0		6.5	4.2	
3b		10.4	13.6		4.6	3.8
4	5.5	12.4		6.9	7.3	
5	2.4	6.9		8.1	6.9	
6	4.7	14.9	20.2	6.6	12.1	9.1
7	10.7	10.4	10.4	4.5	5.8	5.3
8	5.2	8.6	10.0	10.8	9.1	7.9
9	5.9	4.7	7.2	5.3	4.8	2.4
Mean	4.9 ± 2.4	8.4 ± 3.4	10 ± 5.4	6.8 ± 1.7	7.7 ± 2.7	6.3 ± 2.9
P-Value (vs pre-op)		0.03	0.14		0.47	0.77
P-Value (vs post-apm)			0.52			0.39

Blank spaces represent instances in which a measurement was unavailable

Table 3-3 Contact area, all specimens

Specimen Number	Contact Area (mm^2)					
	Medial Compartment			Lateral Compartment		
	Pre-op	Post-apm	Post-impact	Pre-op	Post-apm	Post-impact
1	251	44.4		251	247	
2a	247	222		227	219	
2b		196	200		259	260
3a	330	259		264	256	
3b		216	222		219	191
4	259	194		256	226	
5	268	117		206	198	
6	242	133	108	280	244	241
7	224	176	159	240	213	213
8	232	66.0	70.8	222	205	198
9	224	174	181	218	206	174
Mean	252 ± 32.5	163 ± 66.5	156 ± 57.2	240 ± 24.1	226 ± 21.5	212 ± 32.3
P-Value (vs pre-op)		0.001	0.14		0.14	0.77
P-Value (vs post-apm)			0.92			0.49

Blank spaces represent instances in which a measurement was unavailable

Table 3-4 Center of pressure (CoP) shift, all specimens

Specimen Number	AP CoP Shift (mm)[δ]				Cruciate/Collateral CoP Shift (mm)[+]			
	Medial Compartment		Lateral Compartment		Medial Compartment		Lateral Compartment	
	Pre-op	Post-apm	Post-impact	Pre-op	Post-apm	Post-impact	Post-APM	Post-Impact
1	-2.0		0.6		3.7		1.0	
2a	2.1		-0.6		2.2		1.1	
2b		1.1		0.8		-1.0		-0.5
3a	-2.0		-0.3		2.6		0.9	
3b		0.0		-0.1		0.0		0.6
4	-1.2		-0.5		1.8		1.5	
5	-2.2		0.0		3.9		1.0	
6	-1.0	-1.1	-0.3	0.2	1.9	0.1	2.9	-0.7
7	1.0	-2.7	-0.2	-0.1	1.7	-0.3	0.8	-0.3
8	0.6	0.0	-0.6	-0.1	3.7	-0.1	1.7	0.6
9	0.0	0.0	-0.3	-0.3	2.0	0.1	0.8	0.5
Mean	-0.52 ± 1.5	-0.45 ± 1.3	-0.24 ± 0.37	0.066 ± 0.39	2.6 ± 0.89	-0.19 ± 0.43	1.2 ± 0.68	0.036 ± 0.58
P-Value (vs pre-op)	0.66	0.71	0.85	0.54	0.004	0.10	0.03	0.15
P-Value (vs post-apm)		0.81		0.96		0.84		0.95

Blank spaces represent instances in which a measurement was unavailable
δ positive indicates a posterior CoP shift, negative indicates an anterior CoP shift
+positive indicates a CoP shift towards the cruciate ligaments; negative indicates a CoP shift towards the collateral ligaments
*CoP shift p-values calculated from position, not shift

When the impact gun was used to deliver a 1.2-J impact to the sheep knee articular cartilage, it consistently created a cartilage lesion without damaging the subchondral bone (Figure 3-8). However, despite the visibly depressed cartilage after impact, the addition of this focal cartilage defect did not significantly change contact stress, contact area, or the location of the CoP relative to the changes after partial meniscectomy (Table 3-1). Perhaps this was due in part to the relatively small area of impacted cartilage (28.3 mm^2) relative to the total medial contact area in the intact (series mean = 252 mm^2, SD = 32.5 mm^2; from Table 3-1) and partially meniscectomized (series mean = 163 mm^2, SD = 66.5 mm^2; from Table 3-1) knee. This amounts to ~11% and ~23% of the total area, respectively.

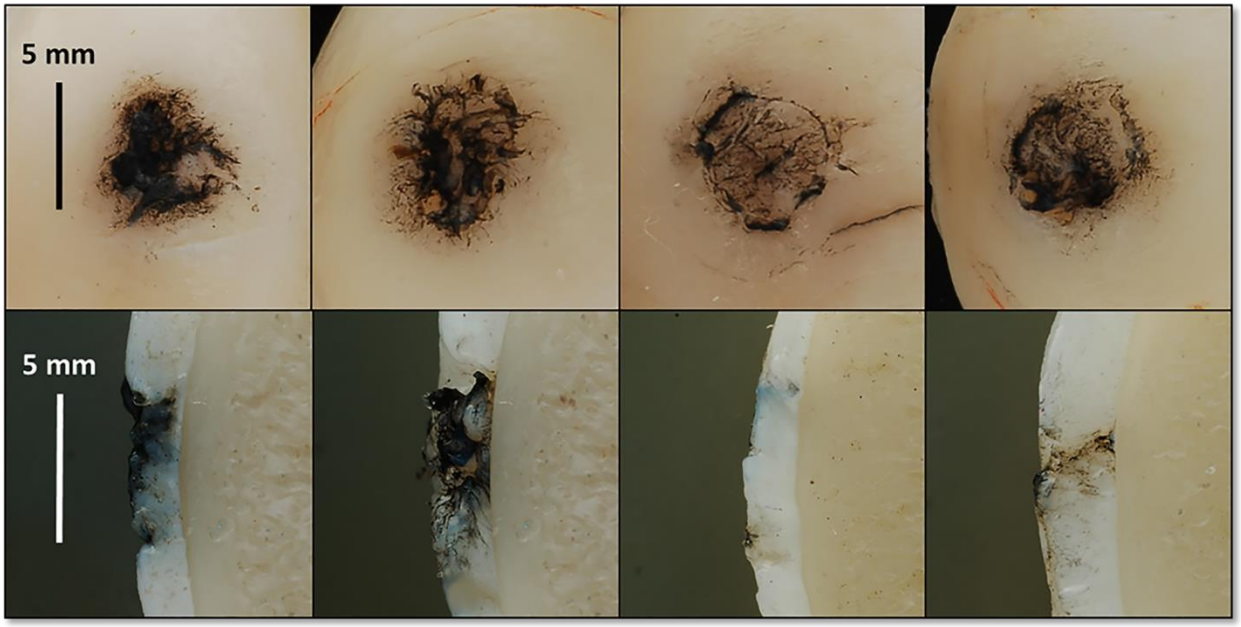

Figure 3-8 (top row) Axial view of four 1.2-Joule cartilage impacts. (bottom row) Corresponding sagittal views following bisection of the impact site. Specimens were photographed under equivalent lighting conditions and positioning. India ink has been used to emphasize cartilage damage.

3.2 Surgical Methods

To investigate the effect of these mechanically characterized cartilage injury methods *in vivo*, a survival-animal MR imaging study of twenty goats was conducted. These goats were drawn from a herd of skeletally mature, castrated male goats bred specifically for research purposes. This study was approved by the University of Iowa Institutional Animal Care and Use Committee (IACUC 5061417) and adhered to Office of Lab Animal Welfare (OLAW) and Animal Welfare Act (AWA) guidelines.

Surgery was performed two to seven days after a pre-operative MR imaging session. Prior to entering the operating room (OR), goat-patients were sedated, intubated, positioned, and prepped for surgery. Special consideration was given to accommodating the quadrupedal goat anatomy in the OR. In order to access the knee, it was necessary to maneuver the goat into a supine position. The head and neck needed to be oriented cranial to (vertically above) the thorax. To meet these criteria, a custom chair (Figure 3-9) was developed by our laboratory's Senior

Engineering Associate, Tom Baer. Once properly positioned, the surgical site was prepared by shaving and sterilizing the operative (left) limb and placing drapes over the remaining non-sterile areas. The surgical team consisted of a surgeon, surgical assistant, and veterinary technician to monitor animal vitals. Support staff assisted with animal transport into and out of the OR, and with collection of photographic and written documentation of the surgical procedures.

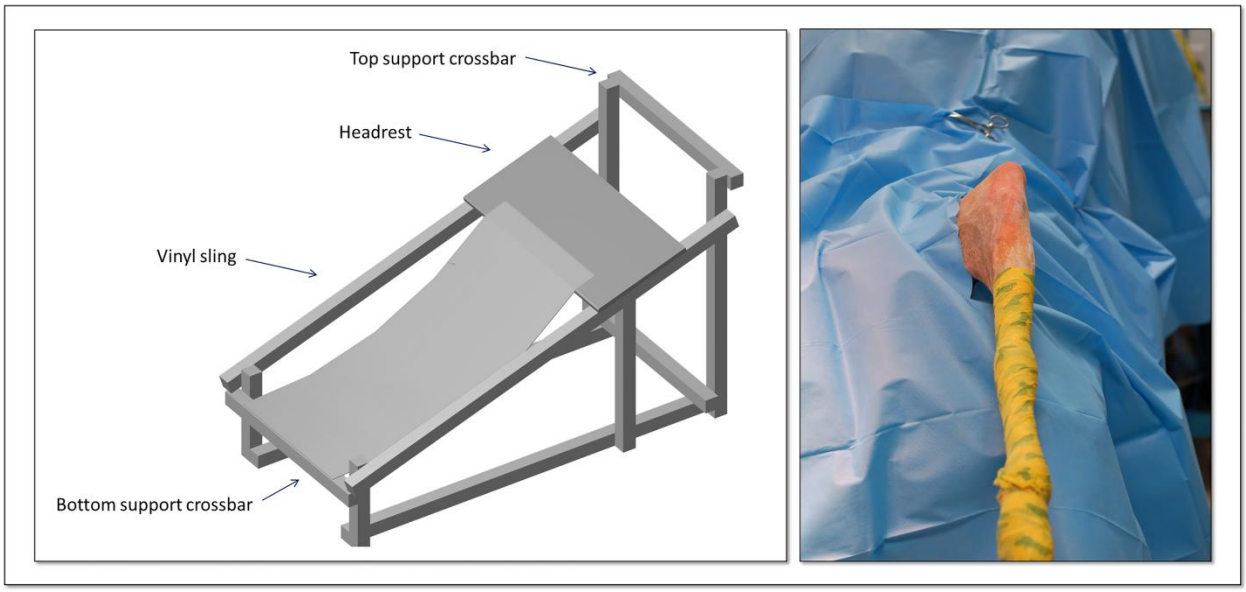

Figure 3-9 In order to properly access the anterior aspect of the knee, it was necessary to position the goats in a supine position during surgery. This required the development of a chair (left). The device is modeled after a deck chair, in which the goat rests on his back on a flexible sling. A headrest supports the back of the head and may be padded. A bottom support crossbar prevents sliding out of the chair. A top support crossbar serves as an anchor point for the horns to prevent cranial shifting during surgery and ensure patency of the airway. The sling is composed of vinyl and conforms to the unique shape of the goat thorax. The crossbars and supports are composed of steel. This device may be sterilized prior to and following each surgery. An additional level of safety is added in the surgical suite by draping the non-operative areas in sterile draping and wrapping the distal operative limb (right).

Surgery began with an anteromedial arthrotomy of the left stile. The approximately 2" incision penetrated the joint capsule, exposing the medial meniscus. A 5-mm wedge of the anterior medial meniscus was excised, providing an unobstructed view of the joint surfaces. To expose the weight bearing cartilage of the medial femoral condyle, the knee was flexed to 100 degrees and stabilized by the surgical assistant. Following a series of practice trials with the impact gun on sterile towels, the surgeon positioned the impact gun perpendicular to the exposed

condylar cartilage and pulled the trigger to deliver an impact. Impact groups were randomized prior to surgery. Six goats received a 1.2-J impact, eight received a 0.6-J impact, and six did not receive an impact. Following impact, the cartilage was visually inspected verify creation of the cartilage defect (Figure 3-10). In a small number of cases, impact damage was visibly asymmetric or the gun slipped/misfired. In those cases, the gun was positioned for a second impact to the same tissue area. A full case summary is documented in Table 3-5. After delivery of a successful impact, the joint was closed in layers using surgical sutures and the goat was transported into a recovery room. Following surgery, animals went on for a 6 month survival period with regular post-operative imaging follow-ups (Figure 3-11). Of the 20 goats enrolled in the study, two required early euthanasia after developing unrelated pathologies.

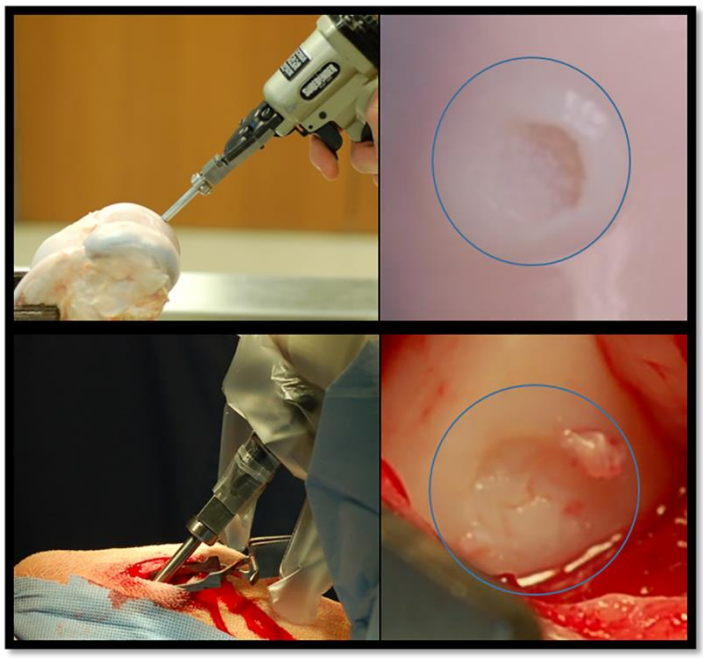

Figure 3-10 This figure illustrates the transferability of impacts performed on the benchtop to those performed *in vivo*. In the upper left panel, the impact gun has been positioned on the weight-bearing cartilage of a bovine femoral condyle. The upper right panel illustrates the resulting cartilage damage (located within blue reference circle). The lower left panel illustrates the positioning of the gun during surgery for delivery of caprine cartilage impacts. Finally, the lower-right panel shows the resulting damage. Note the similarity of cartilage damage *ex vivo* (upper-right) and *in vivo* (lower-right).

Table 3-5 List of surgeries and outcomes by goat number

Goat Number	Impact Group	Outcome
G50001	0.6 J	3 impacts; 2 misfires, followed by 1 clean delivery
G50002	1.2 J	1 impact; clean delivery
G50003	0.6 J	1 impact; clean delivery
G50004	0.6 J	1 impact; asymmetric damage
G50005	0 J	NA
G50006	0 J	NA
G50007	1.2 J	1 impact; clean delivery
G50008	0.6 J	1 impact; clean delivery
G50009	0.6 J	1 impact; clean delivery
G50010	0.6 J	1 impact; clean delivery
G50011	1.2 J	1 impact; clean delivery
G50012	1.2 J	1 impact; clean delivery
G50013	1.2 J	2 impacts; slipped on second impact with secondary trauma
G50014	1.2 J	1 impact; clean delivery
G50015	0 J	NA
G50016	0 J	NA
G50017	0 J	NA
G50018	0 J	NA
G50019	0.6 J	1 impact; clean delivery
G50020	0.6 J	1 impact; clean delivery

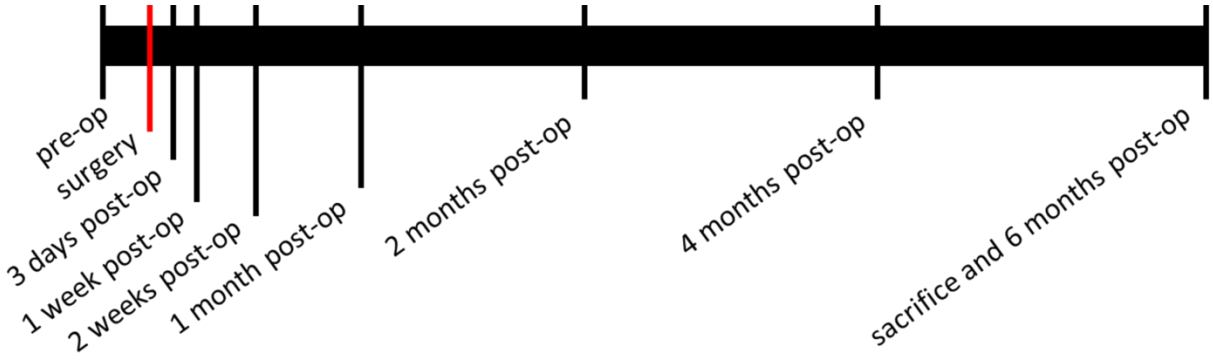

Figure 3-11 Goat-patients were imaged pre-operatively, at postoperative time points of 3 days, 1 week, 2 weeks, 1 month, 2 months, and 4 months, and at time of euthanasia. The surgery has been marked in red.

3.3 Discussion

Characterizing the changes that result from joint trauma is essential to understanding how mechanics contribute to the development of PTOA. This fundamental idea is shared by both clinical and translational research efforts. Both the whole-joint overload induced by partial meniscectomy and the focal cartilage defects created by the impact gun developed in this work are consistent with injuries attributed to the onset of PTOA.

In general, the methodology developed in this work transferred well into the operating room. In a small number of cases, a non-traumatic misfire occurred, requiring repositioning of the gun and a follow-up impact (Table 3-5). There was a 100% survival rate following surgery. Consistent knee flexion prior to positioning the impact gun ensured that each impact was located in the weight bearing cartilage. Although the gun was rigorously tested in the lab to calibrate pressure with energy, the *in vivo* impact energies may have been reduced compared to those found in the lab as a result of dissipation of energy from a less stably supported limb during impact (the surgical assistant stabilized the limb). Drawing upon the knowledge gained from our contact stress measurements, and taking into consideration that lameness was not evident - per the expert opinion of our veterinary staff - we can reasonably infer that the goats continued to load their limbs for the duration of the study.

In conclusion, disruption of the meniscus in a quadrupedal animal knee increased and shifted peak contact stresses on the articular surface, whereas addition of a well-controlled focal cartilage defect had little additional effect on joint contact mechanics. The joint overload and focal articular cartilage injuries mechanically characterized here have numerous applications, including longitudinal study of PTOA development after joint injury and evaluation of a variety of biochemical and surgical treatment options for cartilage defects. The following chapter will discuss the use of imaging to measure changes in cartilage thickness.

CHAPTER 4: IMAGING METHODS & ANALYSIS

This chapter describes the methods and results of multimodal cartilage imaging and thickness measurement. Unfortunately, despite the expectation that cartilage damage would have propagated throughout the joint at 6 months post-injury, photographic evidence obtained during dissection strongly suggested that osteochondral damage was limited to the medial tibiofemoral compartment, specifically the weight bearing region of the femoral condyle (Figure 4-1). Since changes in cartilage morphology are a hallmark of OA and integral to any mechanistic conclusions or validation of compositional biomarkers, our analysis began with the measurement of MRI-derived cartilage thickness in the medial femoral condyle. To investigate the accuracy and precision of these quantitative measures, we performed replicate operations using micro CT.

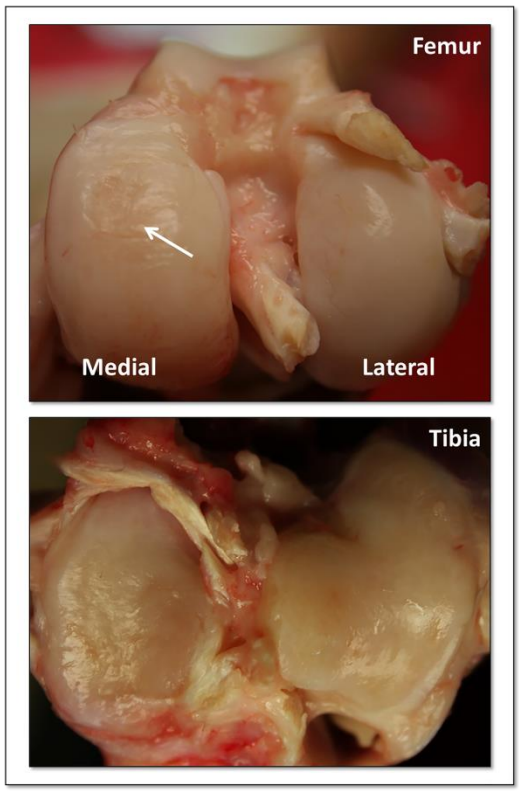

Figure 4-1 Photographs of the femoral condyles and tibial plateaus at time of dissection. Note that the impact site is visible on the medial femoral condyle (white arrow). Notably, the other compartments do not feature visible cartilage damage (e.g. fibrillation, thinning).

4.1 MRI imaging and segmentation

To longitudinally track the features of trauma and disease onset produced by surgically induced trauma, goats underwent common clinical knee diagnostic and morphological MRI preoperatively and at 3, 7, 14, 28, 56, 112 days. All scanning sessions were conducted at The University of Iowa on a 3-Tesla Siemens TIM Trio research platform. The clinical sequences that were acquired included morphometric T1, T2, and Double Echo Steady State (DESS) sequences as well as diagnostic T1ρ. (Figure 4-2; voxel sizes are listed in Table 4-1). These sequences were selected to match those utilized for clinical study of ACL rupture patients. [102] Use of a body coil (Siemens Healthcare, Erlangen, Germany) during acquisition permitted both knees to be imaged simultaneously (Figure 4-4). Each scanning session lasted approximately 1 hour. Goats were euthanized at 168 days (6 months) after surgery. Immediately following euthanasia, hind limbs were disarticulated at the hip and underwent a final MRI session. Each of these sessions also were approximately one hour in duration, but were performed on one knee at a time with a knee coil (Siemens Healthcare, Erlangen, Germany) (Figure 4-4). As noted in Table 4-2, the knee coil and increased scan time permitted morphometric acquisition of a higher, more isotropic image resolution.

Table 4-1 Voxel Spacing of the MRI Sequences Acquired During the Goat Study

Sequence Name	Pixel dimensions (mm^2)	Slice Thickness (mm)
T1	0.44 x 0.44	3.5
T2 FSat	0.44 x 0.44	2*
T1rho	0.63 x 0.63	4
TRUFISP (BONE)	0.44 x 0.44	0.5
DESS	0.63 x 0.63⁺	0.62

*T2 slice thickness was refined from 3.5 mm to 2 mm following the first month of scanning. This approximated to the the pre-op scans of the first eight goats to enter the study.
⁺Resolution acquired at time of euthanasia with knee coil. For the body coil scans, in-plane resolution was 0.86 x 0.86 mm^2.

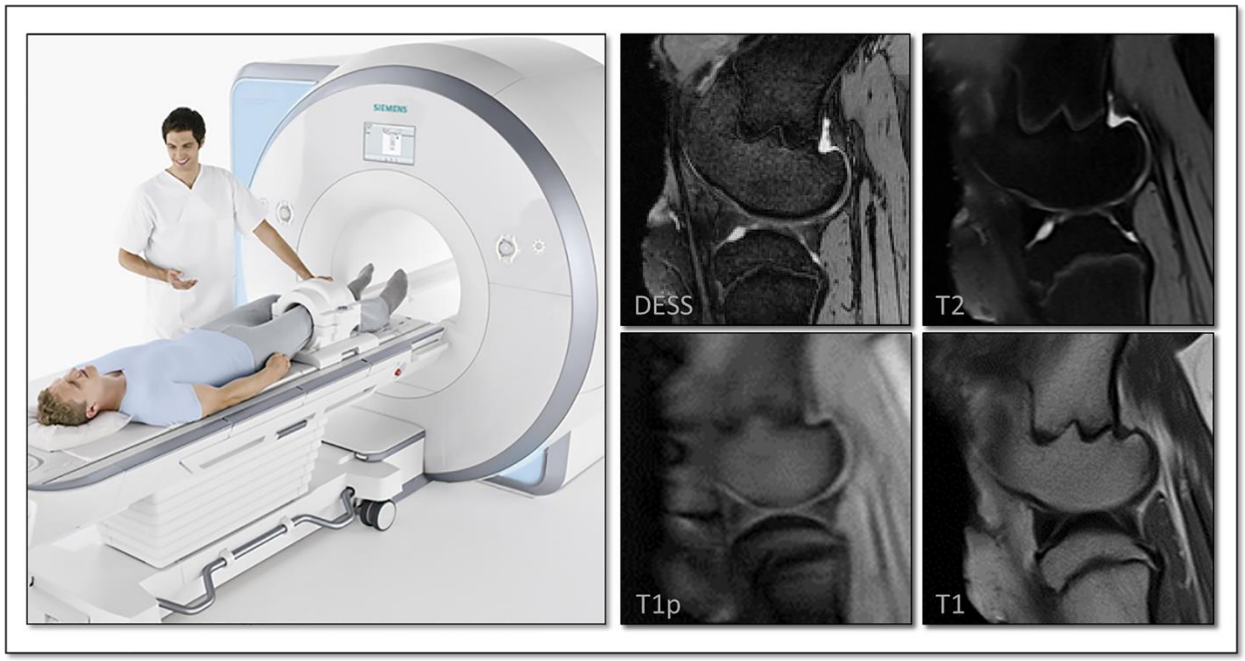

Figure 4-2 A 3-Tesla Siemens MRI scanner equivalent to the one utilized in the goat study is depicted at left. In the right panel, representative images from an equivalent location in the in the goat medial condyle are presented for T1, T2, T1p, and DESS sequences. These images were acquired using a phased array knee coil at time of euthanasia.

Table 4-2 Differences between the *in vivo* and post-mortem morphometric scan (DESS) parameters

Parameter	Units	3D DESS* (*in vivo*)	3D DESS * (post-mortem)
TR/TE	[ms]/[ms]	14.67/4.11	13.27/4.11
In-plane resolution	[mm x mm]	0.9 x 0.9	0.6 x 0.6
Slice Thickness	[mm]	0.6	0.6
Flip Angle	[^{O}]	25	25
NEX (number of excitations)		1	2
Distance Factor	[%]	20	20
Bandwidth	[Hz/Px]	252	252
Basic Resolution	px x px	512 x 512	320 x 320
TA (acquisition time)	[min:sec]	7:04	19:46

***Whereas *in vivo* scans were performed with a body coil, a knee coil was utilized for all post-mortem scans**

1-2 pairs of goats were scanned on any given imaging day. Animals were transported to a ready room in which one animal at a time was sedated and intubated. Anesthesia was maintained

with isoflurane (~1.5%) in oxygen delivered by endotracheal tube. Next, the anesthetized goat was positioned prone on a draped patient transport board (AliMed, Dedham, MA) with the fore and hind limbs stretched cranially and caudally, respectively. Foam blocks were used to position the head in an upright posture to maintain airway patency; additional padding around the thorax prevented rolling to one side. A combination of draping and chux around the head and thorax contained body fluids, hair, and dander that would have otherwise contaminated the scanning environment. A padded knee positioning device was fabricated to keep both knees aligned and positioned anatomically (Figure 4-3).

Immediately prior to scanning, the anesthetized goat was fully draped, transported down a hallway on a gurney, and shifted to the scanner bed, with the hind limbs oriented towards the scanner bore. A Siemens body coil was positioned around both knees (Figure 4-4) and the bed was moved into the bore. In no case did the goat's horns prevent the scanner bed from being positioned completely in the magnetic field, although there were a few instances during which an adjustment of the padding to lower the head was required (Figure 4-3). A veterinary technician or other trained observer was present in the scanning suite during scan sessions to monitor vitals and maintain anesthesia. Following scanning, the goats were returned to their transports, taken off anesthesia, and permitted to slowly return to a wakeful state. Total time under anesthesia varied from 1.5 to 2 hours, with scan time lasting about one hour per goat.

Following the postoperative scanning and gross dissection, the distal 1/3 of the femur and proximal 1/3 of the tibia were placed in formalin fixation for histological processing.

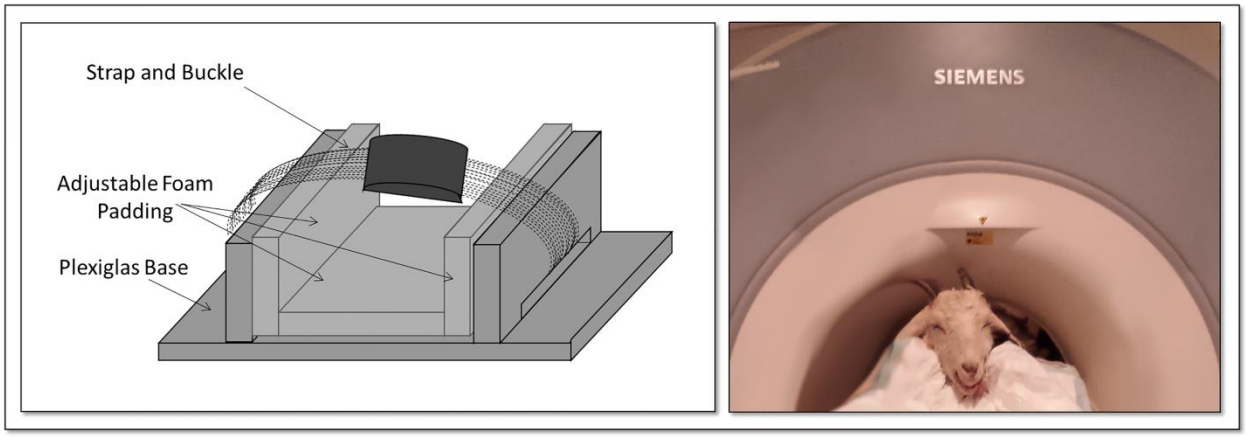

Figure 4-3 In order to position both knees in a common anatomical orientation prior to scanning, a knee positioning device was developed (left). The device is made of a pair of Plexiglas guides attached to a Plexiglas base. Prior to loading the knees, foam padding is added to provide comfort. The knees are positioned prone and level with one another. To secure the position, a strap is run across both knees and locked in place with a plastic buckle. The goats were positioned on the scanner bed and brought into the magnetic field knees-first (right). In many cases, fully sliding the scanner bed into the field brought the horns into contact with the scanner. In a number of cases, the head was repositioned to accommodate the scanner dimensions.

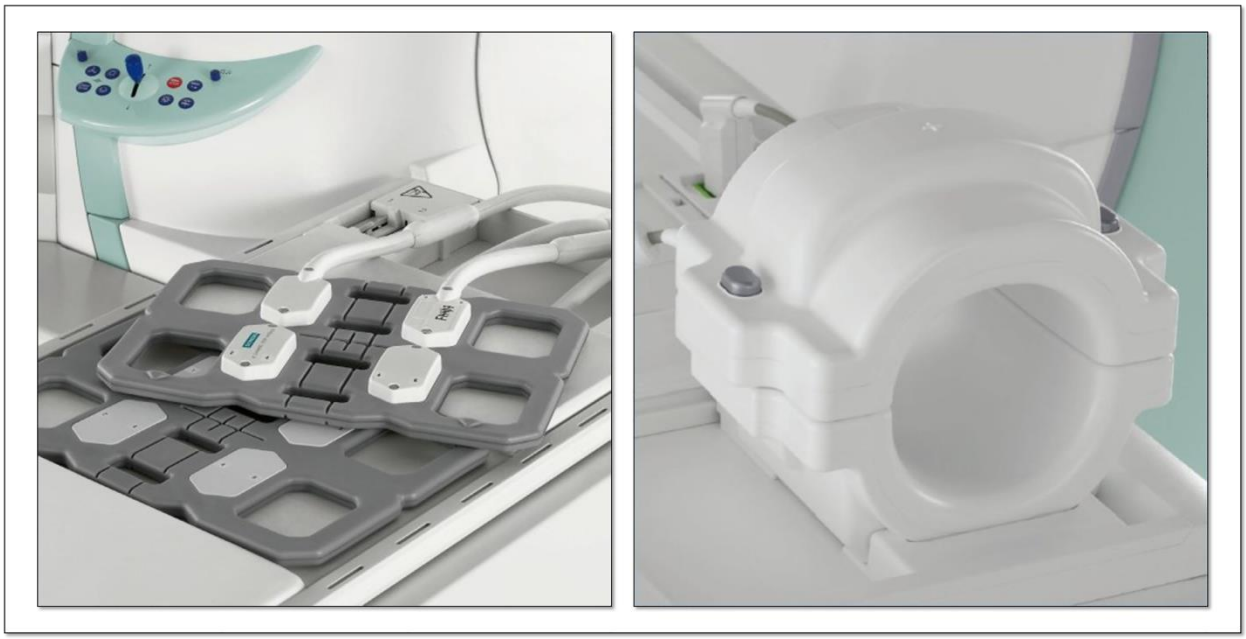

Figure 4-4 Siemens 6 Channel Body Coil (left panel). [103] This coil facilitated scanning of both knees with the full diagnostic and morphological protocol while keeping scan session to 1 hour in duration. It was used for all scanning time points except 168 days postoperative, or the post-euthanasia scan session. Siemens 15 Channel Knee Coil (right panel). [104] This coil was used to scan one knee at a time at the 168 days postoperative time point. For these scans, 1 hour was allocated per knee.

MRI images acquired for this study were segmented manually from the double echo steady state (DESS) sequence at 6 months postoperative. Manual segmentation in a sagittal plane is a widely accepted, validated methodology to accurately segment knee cartilage. [50, 105]

Considerations that factored into which morphometric sequence and time point to select included: (1) the high bone-cartilage contrast conferred by DESS and (2) the importance of identifying end stage OA within the study duration in order to correlate imaging features with the onset and progression and OA. Furthermore, isotropic voxel sizing acquired at 6 months permitted orthogonal reslicing of the transversely acquired slices into a sagittal plane. This operation was performed using the OsiriX DICOM Viewer (Pixmeo, Geneva, Switzerland).

Manual segmentation was performed in Osirix on a slice by slice basis. The structures of interest were the medial femoral cartilage, medial femoral bone, medial tibial cartilage, and medial tibial bone, and each segmented feature was labeled with a unique identifier. A representative sample of a pair of femoral cartilage and bone segmentations can be seen in Figure 4-5. Segmentation of the tibial and femoral bone surfaces was accomplished by two trained members of the Iowa Orthopedic Biomechanics Lab. These bony segmentations were reviewed and manually adjusted as needed by this author. Finally, this author performed the cartilage segmentations himself. Both the operative (left) and non-operative (right) medial compartments were segmented.

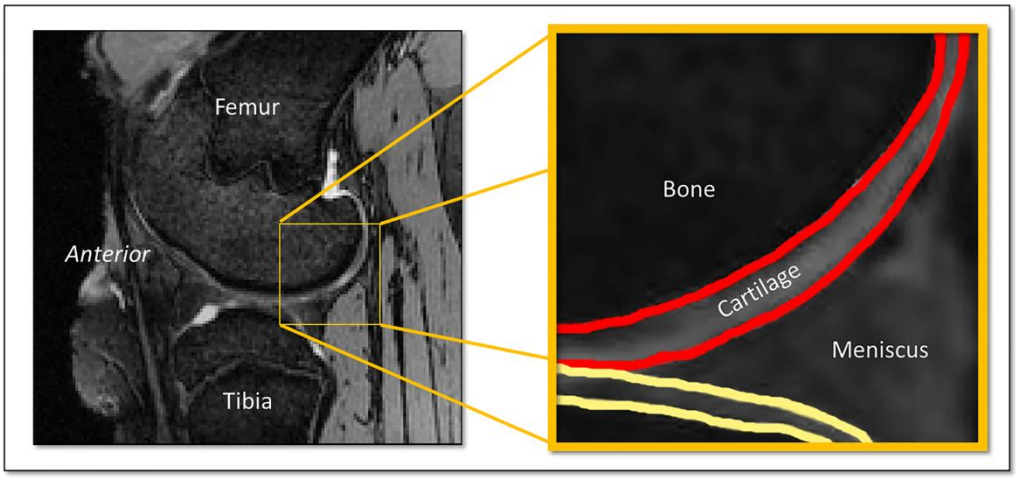

Figure 4-5 Segmentation of subchondral bone and cartilage layers from sagittal reconstructions of DESS images. Femoral contours are marked in red and tibial contours are marked in yellow. A magnified section of the posterior medial tibiofemoral compartment has been provided. These segmentations were performed manually on a slice by slice basis.

In addition, in all cases of blunt impact trauma during surgery, the impact site was identified. First, sagittal slices in the medial tibiofemoral compartment with visible bone marrow lesions, cartilage fissuring, or subchondral bone incongruities were identified. In all cases, these criteria were evident on a series of adjacent slices. In each identified sagittal section, a single point was placed along the bone-cartilage interface corresponding to the center of this damage. The resulting segmentation thus approximated a line connecting these points. When translated into 3D space coordinate space, the centroid of these points corresponded to the center of the real impact site.

In OsiriX, each segmented feature is represented as a collection of discrete Cartesian coordinates with a unique (user-set) identifier. On a knee by knee basis, these features were exported as a single comma separated variable (.csv) file, wherein each line contained a feature label as well as the corresponding xyz coordinate. A MATLAB (Mathworks, Natick, MA) script parsed in each file and separated each feature into a uniquely labeled VTK file (Visualization Toolkit, Kitware, Clifton Park, NY) of ASCII data.

4.2 Micro CT imaging and segmentation

After several months in formalin fixation, the femoral condyles and tibial plateaus were transferred to water and separated into their respective medial and lateral compartments to facilitate micro CT scanning (Skyscan 1176, Bruker, Billerica, MA). Separation of medial and lateral compartments was performed to meet the physical constraints of the Skyscan 1176 bore; specimen dimensions can be no longer than 200 mm and no wider than 68 mm. Only the medial femoral condyle and medial tibial plateau underwent micro CT scanning.

Immediately prior to microCT scanning, each specimen underwent a soak in 30% Hexabrix (Guerbet, Villepinte, France)/70% phosphate-buffered saline (PBS) solution. Hexabrix

is an iodine-based, ionic, low-osmolarity, low-viscosity FDA-approved radiopaque medical imaging agent commonly delivered intravascularly to visualize internal organs and vessels of the human body. When permitted to fully equilibrate into joint tissues, Hexabrix enables visualization of cartilage morphology and composition. The extent to which Hexabrix permeates cartilage is dictated by charge. As a negatively charged imaging agent, Hexabrix is repelled by areas of high proteoglycan (high negative charge) content and permeates preferentially into areas with lower proteoglycan content. In healthy cartilage, this presents as a higher Hexabrix concentration in the superficial zone and lower concentration in the deep zone. As proteoglycan depletion occurs during progression of OA, greater concentrations of Hexabrix permeate into the deeper zones of cartilage. Previous work has identified 20-40 % Hexabrix in PBS as optimal for providing sufficient contrast between cartilage and bone. [44]

For imaging the goat specimens, the soak times used were 6 hours for each condyle and 3 hours for each plateau. These times were selected based on the results of a sequential test of soak duration from 2 to 8 hours in 2 hour increments (Figure 4-6). The objective of that exercise was to identify the minimum time required for the contrast solution to fully equilibrate in goat femoral and tibial cartilage. Full equilibration was defined as the point at which Hexabrix has preferentially distributed throughout the cartilage (heterogeneous signal intensity through the full cartilage thickness) without oversaturation (high homogeneous cartilage signal) or undersaturation (low homogeneous cartilage signal). Saturation level was evaluated by comparing representative images from each time point. 25 mL of solution was found to be sufficient to fully submerge each femoral and tibial specimen during the soak process.

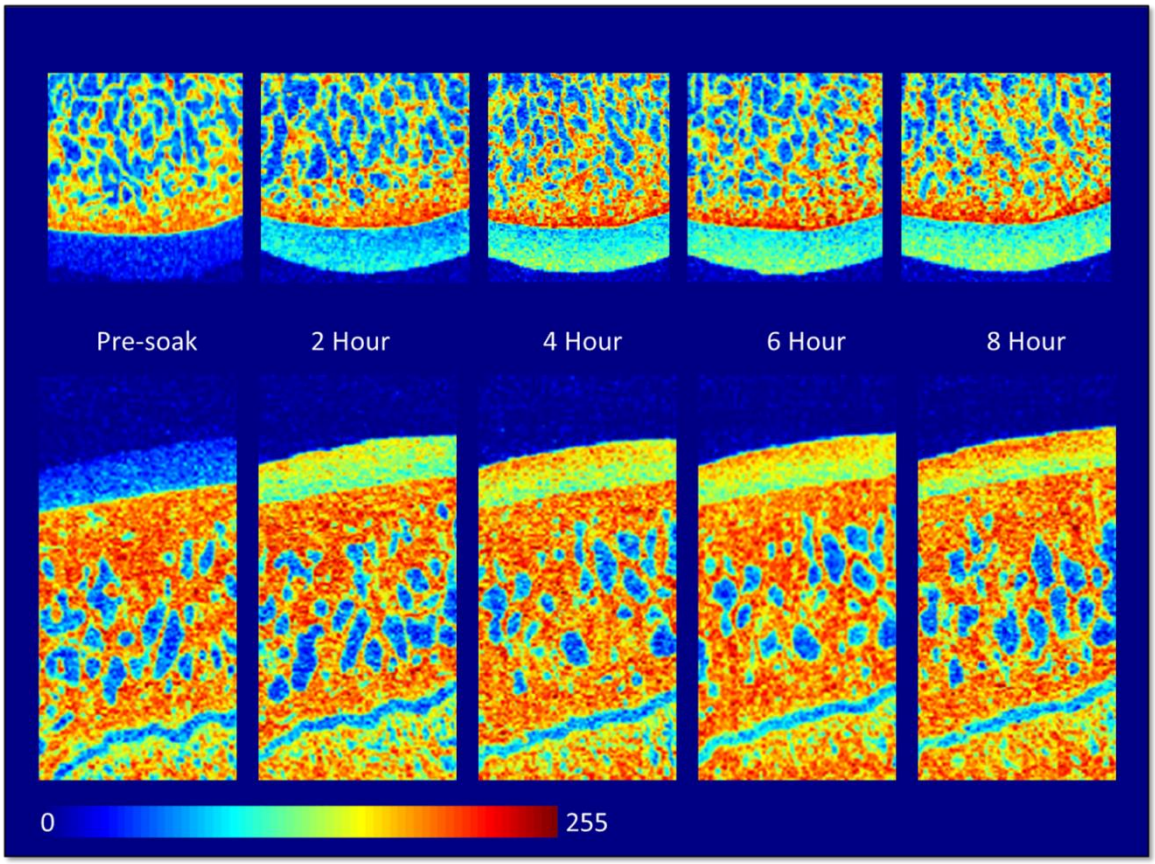

Figure 4-6 In order to determine optimal soak time, a series of compounded contrast soaks were performed. Since the aim of this microCT imaging was to yield high resolution cartilage morphology, the objective of this testing was to identify the minimum time to adequately visualize the cartilage and subchondral bone layers. Future work to evaluate cartilage composition could perform a convergence analysis to determine which soak time resulted in full cartilage saturation with contrast. A pair of condyle and plateau specimens was imaged with contrast and at soak intervals of 2, 4, 6, and 8 hours. From this exercise, soak times of 6 hours and 4 hours were established for the condylar and plateau specimens respectively.

Immediately following soaking, the specimens were removed from the Hexabrix solution, placed in a microCT scanning tray with damp gauze, sealed to maintain a humid environment, and transferred to the scanner bed (Figure 4-7). Scan resolution was set to 9 x 9 x 9 micrometers, the maximum possible scanner resolution. Although this level of resolution isn't quite large enough to meaningfully visualize chondrocytes (~20 μm) or other cartilaginous structures including collagen and proteoglycans, it maximizes the number of cartilage voxels acquired, improving the accuracy of follow-up measurements of cartilage morphology and composition. An Aluminum-Copper (Al-Cu) filter with scanner defaults was selected to provide sufficient

bone-cartilage contrast. Using these settings, acquisition of a single sub-scan required approximately 40 minutes. However, a single sub-scan was insufficient to fully capture the articular cartilage surface of each specimen. In Skyscan 1176 parlance, “oversize” scanning refers to the imaging of specimens greater than 22 mm long and “offset” scanning refers to the imaging of specimens wider than 35 mm. While oversize scanning consists of a series of overlapping sub-scans along the length of the scanner, offset scanning is accomplished by acquiring a pair of sub-scans width-wise for every sub-scan lengthwise. Therefore, oversize scanning increases scan time directly as the function of the number of required sub-scans and scanner offset doubles scan time. To minimize scan time (and image set size) we endeavored to limit our scanning area to 2-3 oversize scans without offset. This limited total scan time to either 1 hour 20 minutes or 2 hours per specimen.

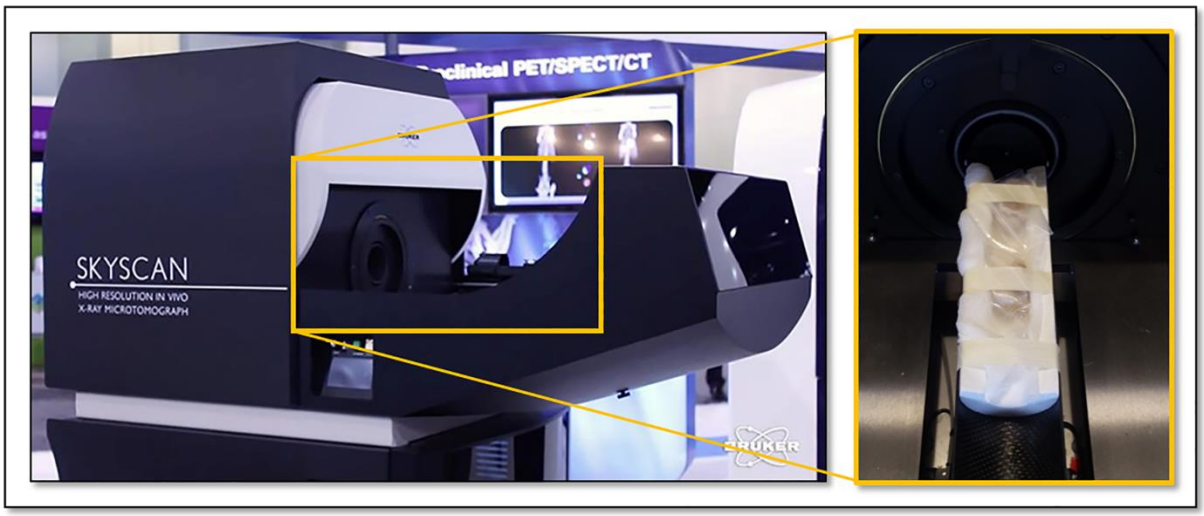

Figure 4-7 Skyscan 1176 micro CT scanner (left). The bore and scanner bed have are contained in the orange box. During scanning, a cover (currently retracted) protects the scanning environment from exposure to particulate matter in the air. A magnified view of the scanner bore (right). A specimen has been positioned on a bed of moist gauze on a Styrofoam scanning tray, wrapped in saran wrap, and placed on the scanning bed.

After acquisition, images were reconstructed using software from the scanner manufacturer (Bruker, Billerica, MA). This process converted the approximately 2000-3000 acquired projections into a stack of about 4000 coronal cross sections. [106] Several

reconstruction parameters were fine tuned to enhance the background-cartilage-bone contrast. To identify the appropriate settings, the manufacturer software uses a guess and check method wherein the user generates a series of test images with a range of values of a single parameter and evaluates which image is best. Noise was reduced with a 5x5 Gaussian smoothing filter (smoothing level of 4). Malalignment compensation was set to -64 to compensate for possible misalignment during acquisition. This parameter for corrects for tails, blurring, and doubling of structure. Ring artifacts reduction was set to 10 and beam-hardening correction was set to 15%. The output histogram was set from -0.002658 to 0.023627 to standardize the range of gray values corresponding to background, cartilage, and bone. A representative reconstruction protocol log has been attached as an appendix. Output formats provided by the software included the default 8-bit bitmap (BMP, 0-255), 16-bit TIFF (0-655353), 8-bit PNG (0-255), and 8-bit JPG (0-255), and 4-byte floating point format (F4F, 32-bit). Higher bit image types offer a greater range of gray values and are favorable for compositional outcome measures. However, higher bit images require more space to store and more memory to work with, making later processing potentially problematic. Since the focus of the current analysis was cartilage morphology, the default BMP output format was used.

Cartilage was segmented automatically from micro CT scans using a threshold-based algorithm (MATLAB). While MRI segmentation extracted the cartilage and subchondral bone layers individually, the process developed to segment micro CT extracted both features simultaneously. The overarching logic of the algorithm was to generate a solid bone mask, extract the foreground (cartilage & bone), and subtract the bone mask from the foreground. Segmentation was performed without down sampling the reconstructed images. To conserve

memory, segmentation was performed on a slice-by-slice basis by saving and closing each segmentation prior to beginning segmentation of the next slice.

First, the algorithm used two unique hard-coded threshold parameters to separate the original image (Figure 4-8, panel 1) into background, cartilage, and bone layers based on intensity (Figure 4-8, panel 2). These thresholds were optimized specifically for femoral condyle specimens by applying a range of thresholds to a set of test images and selecting the pair of values that best delineated background, cartilage, and bone while retaining edge contours. Once thresholded, the bone label was extracted (Figure 4-8, panel 3) and converted to a binary mask for a series of operations to remove background noise and fill holes. Next, a convex hull was computed around the remaining bone label mask and filled in (Figure 4-8, panel 4). Adding the convex hull to the original bone mask, removing noise, and filling holes effectively created a solid bone mask (Figure 4-8, panel 5).

A single thresholding operation on the original image followed by noise removal and hole filling produced a foreground mask (Figure 4-8, panel 6). Subtraction of the bone mask from the foreground and automatic deletion of small regions produced the cartilage mask featured in Figure 4-8, panel 7. Finally the border pixels of this mask were extracted, resulting in cartilage and subchondral bone surface contours (Figure 4-8, panel 8). This procedure was repeated for every image in a given scan. Batch processing was implemented to enable sequential segmentation of more than one specimen without the need for user interaction.

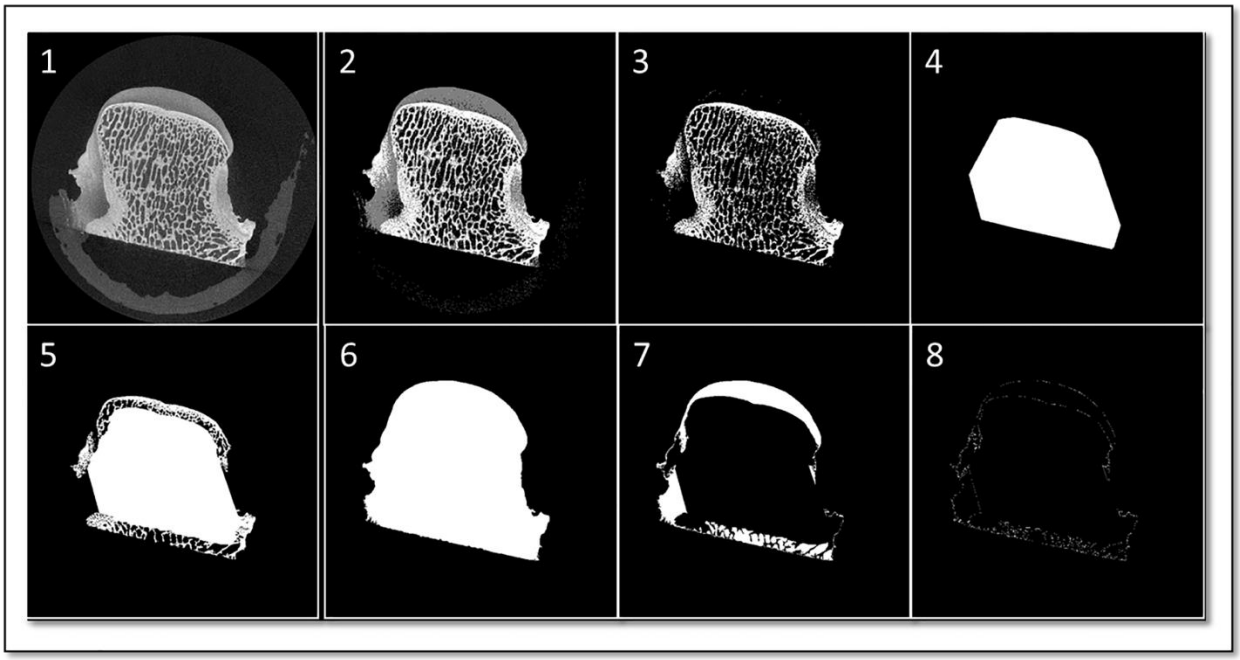

Figure 4-8 Illustration of the steps involved in segmenting cartilage from a single micro CT slice; (panel 1) The original image; (panel 2) Intensity-based separation of bone, cartilage, and background; (panel 3) Extraction of bone label; (panel 4) Calculation of a convex hull following erosion and hole filling steps; (panel 5) Addition of the convex hull back to the original bone mask; (panel 6) Separating foreground from background; (panel 7) subtraction of the bone mask from the foreground; (panel 8) Extraction of border pixels from the cartilage mask.

Following completion of segmentation, the resultant border pixel masks were loaded sequentially into a three column array of image coordinates (column, row, slice). To improve downstream processing speed and facilitate the efficient use of modeling software, points were down-sampled to 1/300th of their original density (every 30th point of every 10th slice), yielding models of approximately three-hundred thousand points. Without down-sampling, a single femoral condyle was composed of over one hundred million unique points. A fully rendered model was generated to confirm that this approximation did not deleteriously affect the curvature of acute surface contours.

Next, the header file generated during image reconstruction was referenced to extract the origin of the scanner coordinate system and voxel dimensions, permitting image coordinates to

be transformed into physical coordinates. Finally, the point clouds representing each cartilage surface were written to unique VTK files.

4.3 Modeling and registration

Each VTK file (MRI & micro CT) was then imported into Geomagic (3D Systems, Rock Hill, SC), wherein a point cloud of each feature was automatically generated. Since each cloud of micro CT points contained both cartilage and subchondral bone layers, these were manually separated and provided with unique labels. In contrast, MRI point clouds had already been uniquely labeled and no additional processing was required. Triangular surface meshes were generated from each labeled point cloud (Figure 4-9) using pre-programmed software functions. These provisional surfaces were converted to an open manifold, which served to eliminate any non-continuous triangles that did not contribute to the articular surface geometry. Next, hole filling was performed semi-automatically as needed to correct any gaps generated during the conversion from points to a surface model. To prevent the hole filling process from attempting to estimate surface curvature, a "flat" filling type was utilized.

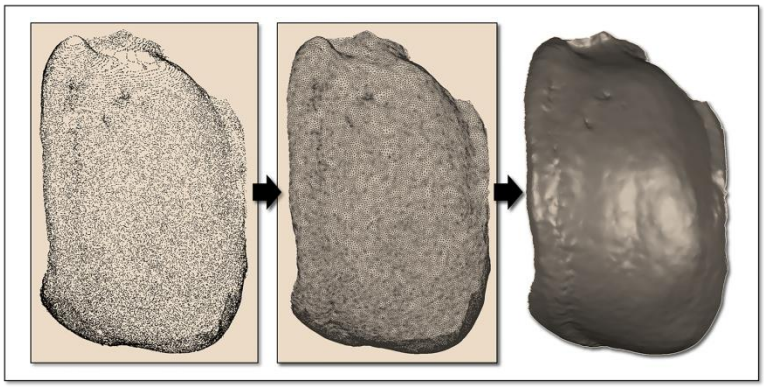

Figure 4-9 Process of generating a surface model. A cloud of points (left panel) is converted into a triangular surface mesh (center panel). When each face of this mesh is filled in, the surface contours are clearly visualized (right panel). This particular surface was derived from microCT.

Stair-step artifact results from discretizing a continuous contour, as occurs during the process of segmenting an image stack on a slice by slice basis. Its effect is to create a ribbed

appearance when a surface model is ultimately generated. The severity of this artifact is directly related to the density of points contributing to the surface. On MRI, slice thickness is the chief determinant of stair-step artifact. As slice thickness increases, the effect of stair-step artifact becomes more pronounced, with visible steps aligned with the imaging plane. Not surprising, this feature was more pronounced on the MRI surfaces than those derived from micro CT. To eliminate stair-step artifact, a pre-programmed function in the software was applied to reduce sharp edges and fill small holes. This was followed by application of a built-in smoothing algorithm.

Surface meshes were refined and decimated to 150,000 elements before undergoing a second round of surface corrections and smoothing using the same Geomagic functions to remove remaining stair-step artifact. These procedures were deemed to sufficient to (1) provide a sufficiently dense mesh to perform thickness calculations and (2) adequately remove the tracings of stair-step artifact. A deviation analysis procedure on original and smooth surface pairs verified that the smoothing procedures were not altering true surface contours. Figure 4-10 provides an illustration of the corrected MRI and micro CT cartilage surfaces compared to the original specimen stained with India ink.

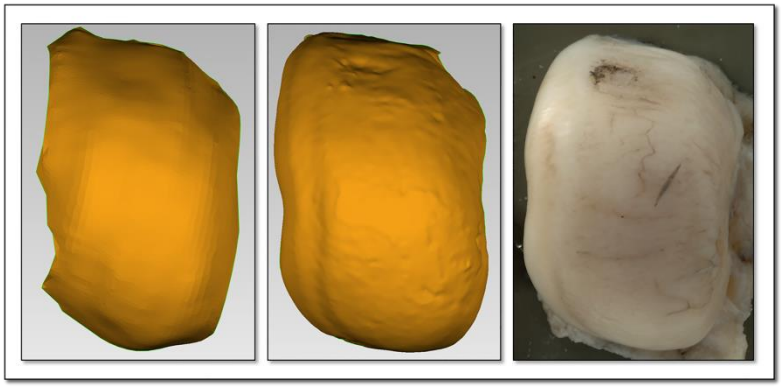

Figure 4-10 Cartilage surfaces derived from MRI (left) and microCT (center) with India Ink-enhanced macroscopic photography (right). Note that the MRI-derived surface grossly matches the actual surface geometry whereas the microCT-derived surface is able to distinguish fine detail.

Surface rendering was followed by registration. Orienting features into the same reference frame enables direct comparisons between imaging modalities or across time points. To better inform the registration process, surface features extending beyond the medial tibiofemoral compartment were manually removed. Next, each medial femoral bone surface was registered to a left goat reference femur acquired using CT imaging. The right surfaces were mirrored to match the reference femur. The reference femur had been oriented anatomically according to a lower extremity example from the literature (Figure 4-11) [107]. The transform necessary to bring the femoral condyle bone surface into alignment with the reference femur was saved and applied to the associated cartilage and impact surfaces as well. This brought all experimental surfaces into a common anatomic (reference) coordinate system which allowed for cartilage thickness to be measured on the same site on both right and left models. Registered surface models were exported from the Geomagic workspace as stereolithography (.stl) files.

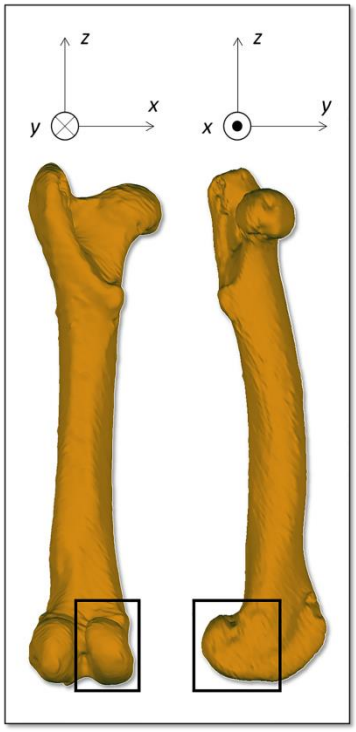

Figure 4-11 Orientation of the reference femur. Adapted from a joint coordinate system defined by Grood et al. for describing three dimensional movements at the knee. [107] All surfaces were registered to this common frame of reference. The boxed region corresponds to the area over which cartilage was segmented.

4.4 Calculating cartilage thickness

For this work, the difference between the articular cartilage surface and the bone/cartilage interface surface was defined as cartilage thickness. Two techniques for measuring the distance between two surfaces were considered: ray casting and nearest neighbor. In the technique of ray casting, a vector is projected from the centroid of each face on a "test" surface (bone) along the surface normal to an opposing "reference" surface (cartilage) The vector length required to intersect the reference surface corresponds to cartilage thickness at that centroid. For the nearest neighbor technique, the Euclidean distance between a centroid on the test surface and the nearest centroid on the reference surface corresponds to cartilage thickness.

There are a number of pros and cons to each technique. For example, ray casting is significantly influenced by the roughness of the test and reference surfaces; increased roughness results in longer than expected projections. Due to the increased resolution (and associated surface roughness) of microCT-derived surfaces, this had a greater effect on microCT-derived cartilage thickness than MRI. Second, the comparative curvature of both surfaces can have a profound effect on both techniques, resulting in longer or shorter than expected thickness measures. To account for these potential sources of error, a number of assumptions were made. For ray casting, thicknesses of greater than 5 mm were not included in the thickness calculations. For the nearest neighbor technique, thicknesses with a critical angle larger than 45 degrees were dismissed.

Two techniques were used to define regions of interest from which to evaluate cartilage thickness. In the first, cartilage thickness was calculated radiating away from the point of impact. This provided a representative measure of the extent to which cartilage thinning had occurred. In the second, weight bearing samples of cartilage thickness were measured, allowing for a direct

comparison of the comparative accuracy and precision of MRI- and microCT-derived cartilage thickness.

4.4.1 Measurement 1: radial thickness measures

This measurement endeavored to characterize cartilage morphology relative to the surgically induced impact trauma. First, a 2-mm diameter cylinder was fit to the centroid of the bone surface nearest the impact centroid, its central axis parallel to the surface normal of the associated face. Next, the average cartilage thickness of all the points within the area defined by the cylinder was calculated. This procedure was repeated for cylinders 4, 6, 8, 10, 12, and 14-mm in diameter (Figure 4-12). For each successive measurement, the preceding points were excluded. This resulted in the measurement of thickness in progressively larger discs radiating away from the impact center. Within-subject comparisons were made between the operative and non-operative knees over the same regions of articular cartilage. With this methodology, significant between-joint differences outside the direct impact zone are indicative of cartilage thinning and the onset of PTOA. For specimens from the 0 J impact group, measurements were made from starting from a location corresponding to the centroid of all the impact sites.

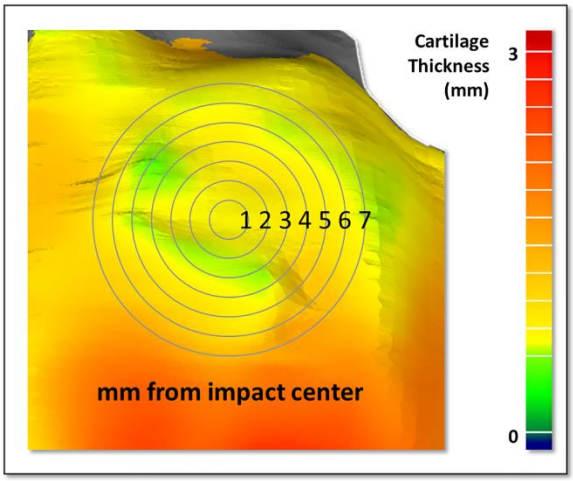

Figure 4-12 Illustration of the region over which radial thickness measurements were made. Annuli were evaluated at intervals of 1-mm radiating away from the impact center to a distance of 7-mm. An average cartilage thickness was calculated for each annulus. This provides a representative measure of cartilage thickness radiating away from the point of impact.

4.4.2 Measurement 2: multi-point analysis of fixed area.

This technique endeavored to characterize whole joint changes by sampling cartilage thickness at a variety of locations throughout the weight bearing region. Since the weight bearing region was not explicitly defined, the impact locations were used as the set of sampling points. Using the same methodology as described above, 2-mm diameter cylinders were defined at each impact point of each specimen. Right-left differences defined as the sum of the difference were evaluated and compared between injury groups. An illustration of the points over which impacts were sampled is depicted in Figure 4-13.

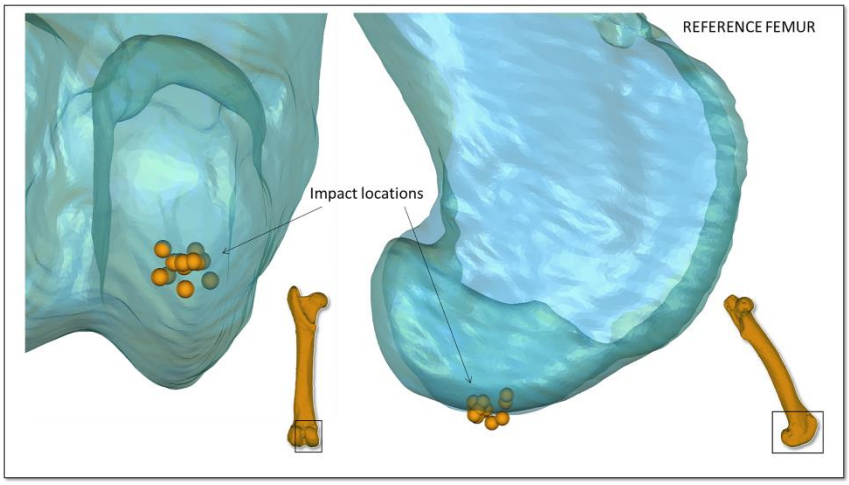

Figure 4-13 Sampling point locations overlaid on reference femur. Each orange sphere corresponds to a unique impact location (note: the spheres depicted in this figure have a diameter of 2-mm). In the sagittal figure, the reference femur has been oriented to the stance phase of gait at approximately sixty degrees of knee flexion. Note that all the points are located in the weight bearing region.

4.4.3 Additional considerations for cartilage segmentation and thickness measurements

To address concerns that may arise from variability in segmentations that could arise from having multiple individuals involved in the segmentation process, interobserver agreement was assessed. To accomplish this, the nearest neighbor differences between bony segmentations performed by each observer were calculated and evaluated at the different radial distances from the impact center. The results of this analysis indicated an average difference of less than 0.1 mm with a standard deviation of approximately 0.05mm. These sub-voxel differences suggest that a

majority of the surface contours overlapped perfectly. A pair of surfaces utilized for this study is presented in Figure 4-14.

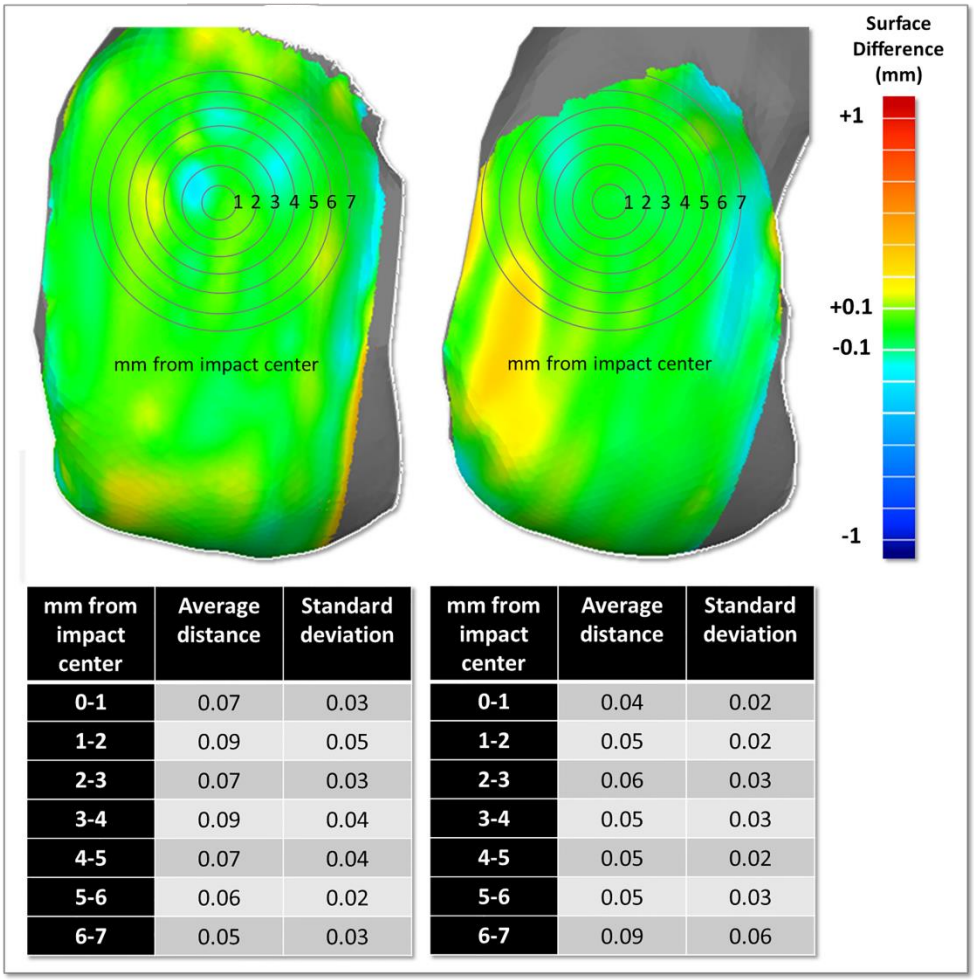

mm from impact center	Average distance	Standard deviation
0-1	0.07	0.03
1-2	0.09	0.05
2-3	0.07	0.03
3-4	0.09	0.04
4-5	0.07	0.04
5-6	0.06	0.02
6-7	0.05	0.03

mm from impact center	Average distance	Standard deviation
0-1	0.04	0.02
1-2	0.05	0.02
2-3	0.06	0.03
3-4	0.05	0.03
4-5	0.05	0.02
5-6	0.05	0.03
6-7	0.09	0.06

Figure 4-14 To ensure the reliability of manually segmented MRI-derived surfaces, interobserver variability was examined. To accomplish this, bony segmentations performed by two trained members of the Iowa Orthopedic Biomechanics Lab were compared. Representative surfaces acquired from a left-right condyle pair are depicted (left surfaces on the left, right surfaces on the right). The colored maps illustrate the surface differences between each observer's segmentations. To quantitatively compare these differences, the average and standard deviation of the distances between surfaces were compared at the various radial locations. The average distance between surfaces within the sampled region was less than one voxel and the standard deviation was near zero. These results indicate that there was low variability between the manual segmentations performed by these trained observers.

Another challenge to accurate segmentation is that there is not a clear boundary between cartilage surfaces in contact with one another (Figure 4-15). This presents a segmentation challenge that is unique to the weight bearing cartilage surfaces of intact joints. Within this work, contacting articular cartilage surfaces were only encountered for MRI-derived cartilage contours,

as the micro CT images were acquired with the joint disarticulated. For segmentation of these contacting areas of tibiofemoral cartilage, the cartilage space was symmetrically bisected during the segmentation process. As suggested by the results of sampling weight bearing cartilage for both modalities, this assumption may have resulted in a uniformly thinner thickness in areas of contact on MRI. However, additional factors may have contributed to this difference, including cartilage compression at points of contact in the intact knee or cartilage swelling as a result of the contrast soak that preceded microCT imaging.

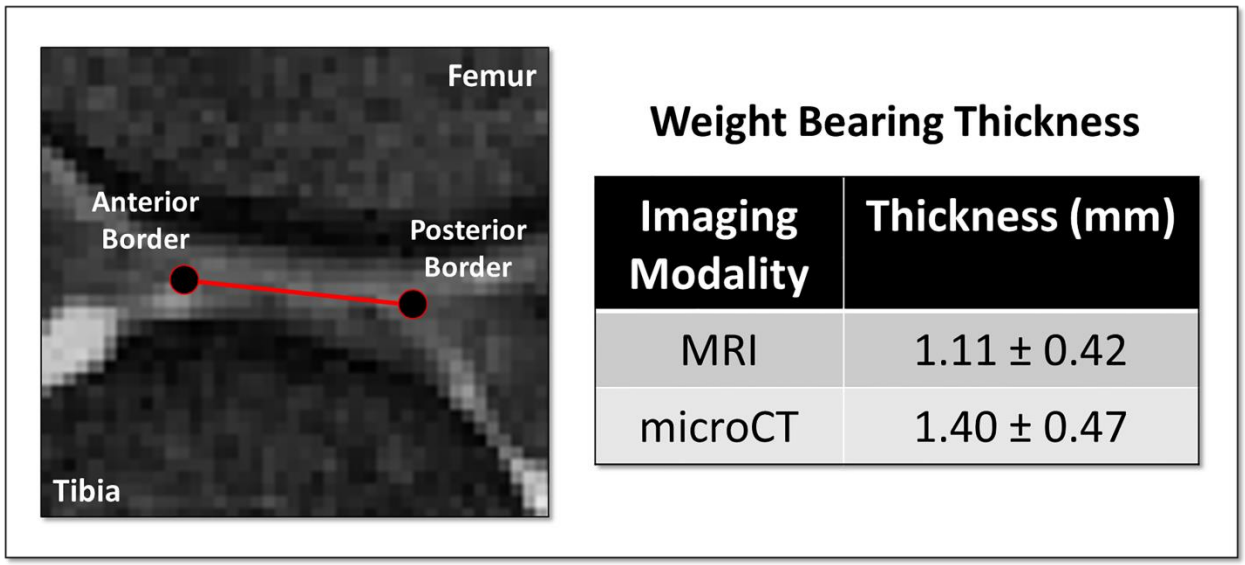

Figure 4-15 Distinguishing the border between cartilage surfaces in contact presents a unique challenge to segmentation of the intact knee (left). To account for this, the anterior and posterior borders of tibiofemoral contact were identified and the contact region was bisected. The absolute average difference in weight-bearing cartilage thickness between MRI and microCT was approximately 0.3 mm (right). This difference may have been influenced by the accommodations made for contact in the intact joint, cartilage compression in the intact joint, or cartilage swelling associated with the contrast soak that preceded microCT imaging.

4.5 Results

Comparison of the results of thicknesses calculated from ray casting versus nearest neighbor indicated that both techniques produced comparable average thickness measures. However, the nearest neighbor technique produced a lower standard deviation within a radially sampled region (Figure 4-16, left). Based on these findings, the results presented in this work are

based on a nearest neighbor technique of calculating cartilage thickness. A representative pair of MRI and micro CT maps of cartilage thickness is depicted in depicted in Figure 4-16 (right).

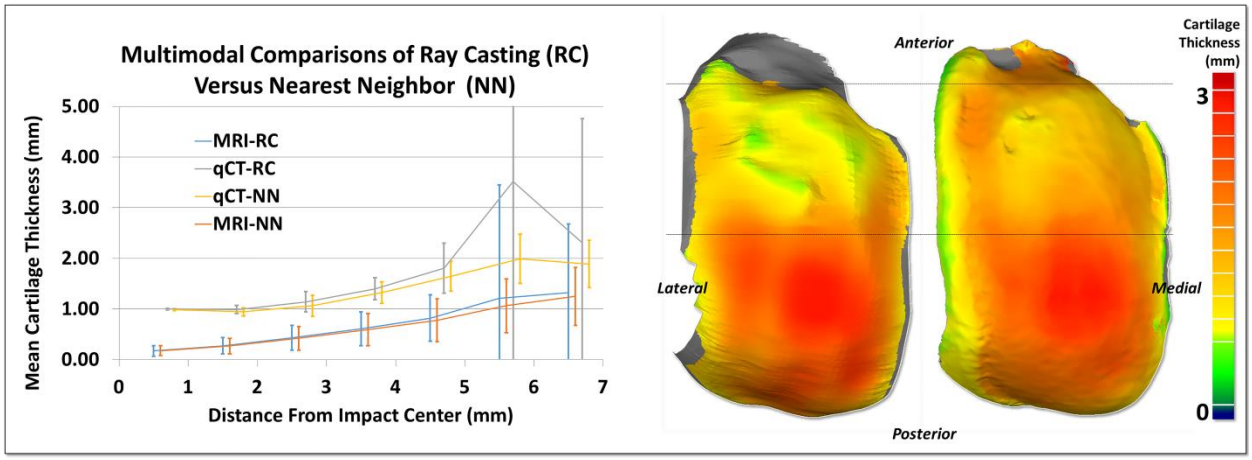

Figure 4-16 Radial thicknesses are presented for a representative pair of MRI- and microCT-derived surfaces (left). Note that ray casting to calculate thickness produces large standard deviations as one approaches the outer boundaries of the cartilage surfaces, although this effect is more pronounced in the microCT-derived measures, demonstrating the effect of increased surface roughness on microCT surfaces. At right, a pair of MRI (left map) and micro CT (right map) cartilage thickness maps are presented. Qualitatively, the microCT thickness map appears to be about 0.5 mm thicker in the weight-bearing region (defined between the two dotted lines). This is quantitatively confirmed by the thicknesses plotted at left.

4.5.1 Radial thickness

Cartilage thickness propagating away from the site of impact was calculated for all MRI-derived models. A plot of radial thickness in operative (left) versus non-operative (right) knees for each goat is presented in Figure 4-17. The region in blue corresponds to the impact zone. Recall that the location sampled on the right knee was spatially equivalent to the region of interest on the left knee. The cartilage thickness was more uniform in the non-operative knee, with limited changes in thickness moving away from the impact site. Next an effort was made to distinguish between injury groups on the basis of radial cartilage thickness. Figure 4-18 depicts left and right knees plots organized by injury group. Asterisks correspond to statistically significant left-right comparisons. P-values were calculated with a paired Student's T test with significance level of 0.05. Notably, left and right thickness differences were statistically significant within the impact zone only. Whereas significant differences occurring outside the

impact zone would have corresponded to cartilage thinning, this was suggestive that the impact injury itself was probably the primary source of the difference.

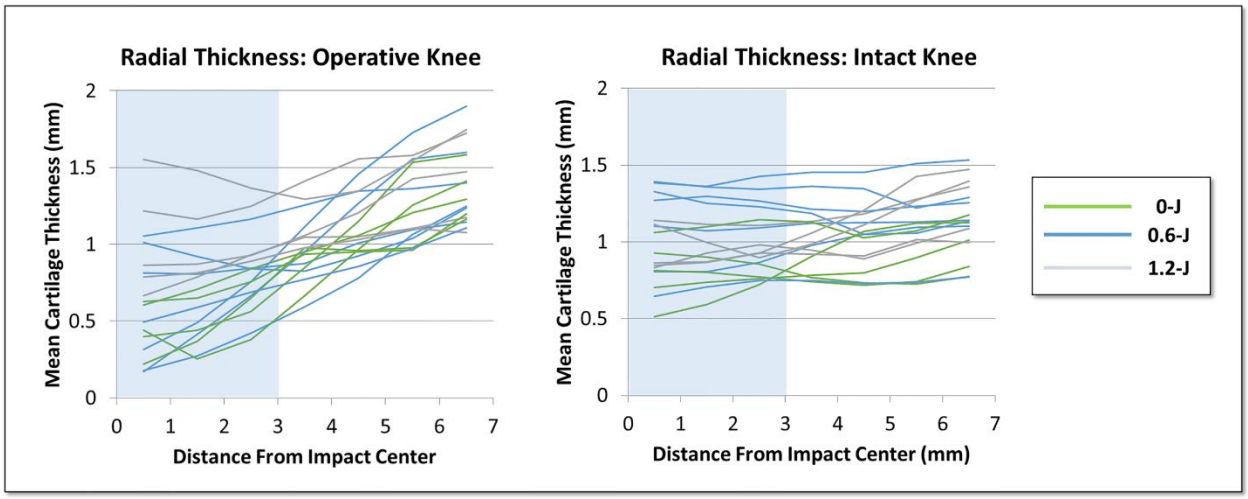

Figure 4-17 Plot of average thickness versus distance from impact center of operative (left) and intact (right) knees- all subjects. The impact zone has been demarcated in blue. Impact groups have been color coded (0-J in green, 0.6-J in blue, 1.2-J in grey). In the operative knee, note that the 0-J impact group had thicker cartilage in the impact zone and did not appear to change appreciably in thickness radiating away from the impact center. In contrast, the 0.6- and 1.2-J impact groups tended to present with reduced cartilage thickness in the impact zone that converged with the 0-J impact group away from the impact site. In addition, note that the thicknesses remained comparatively constant throughout the intact knee.

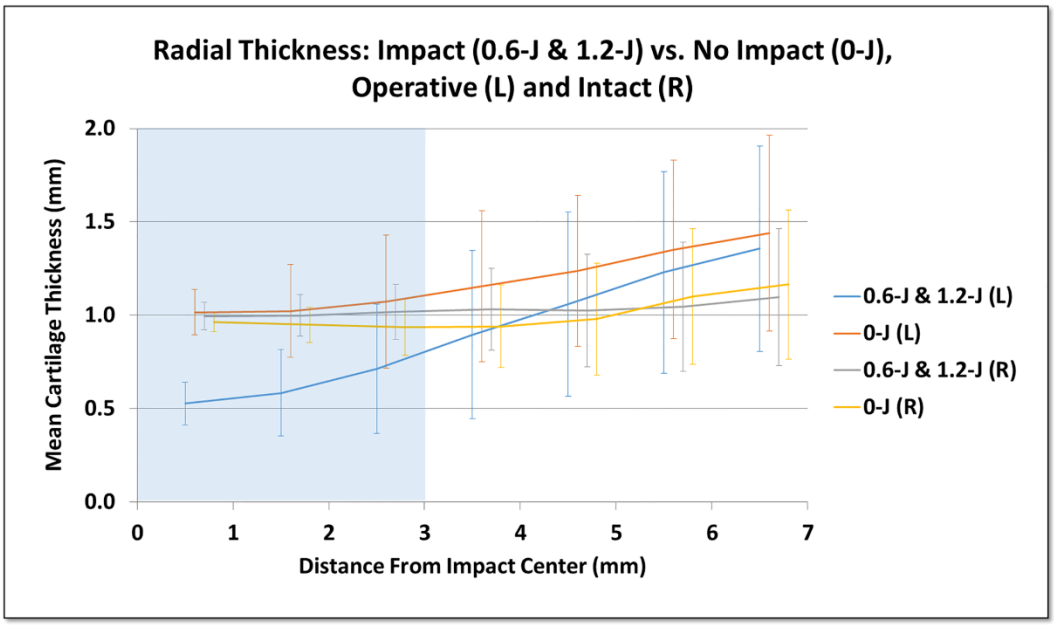

Figure 4-18 Plot of average thickness versus distance from impact center for operative (L) and intact (R) knees, separated by impact (0.6-J & 1.2-J) vs. no impact (0-J). The impact zone is demarcated in blue. Error bars illustrate significant differences between cartilage with impact trauma and all other groups within the impact zone. Outside the impact zone, the groups are not significantly difference. In addition, there was not a significant effect of partial meniscectomy alone on cartilage thickness, as evidenced by the considerable overlap between the 0-J (L) and intact groups.

To investigate the effect of impact versus no-impact in a more general sense, both impact groups were binned together and subjected to additional testing for statistical significance. The results of this comparison are depicted in Figure 4-19. This analysis resulted in p-values closer to zero. This plot clearly illustrates reduced cartilage thickness in the impact zone (recall that the impact zone was a 6-mm diameter circle) and a return to a thickness more akin to that of the operative knee immediately outside of it.

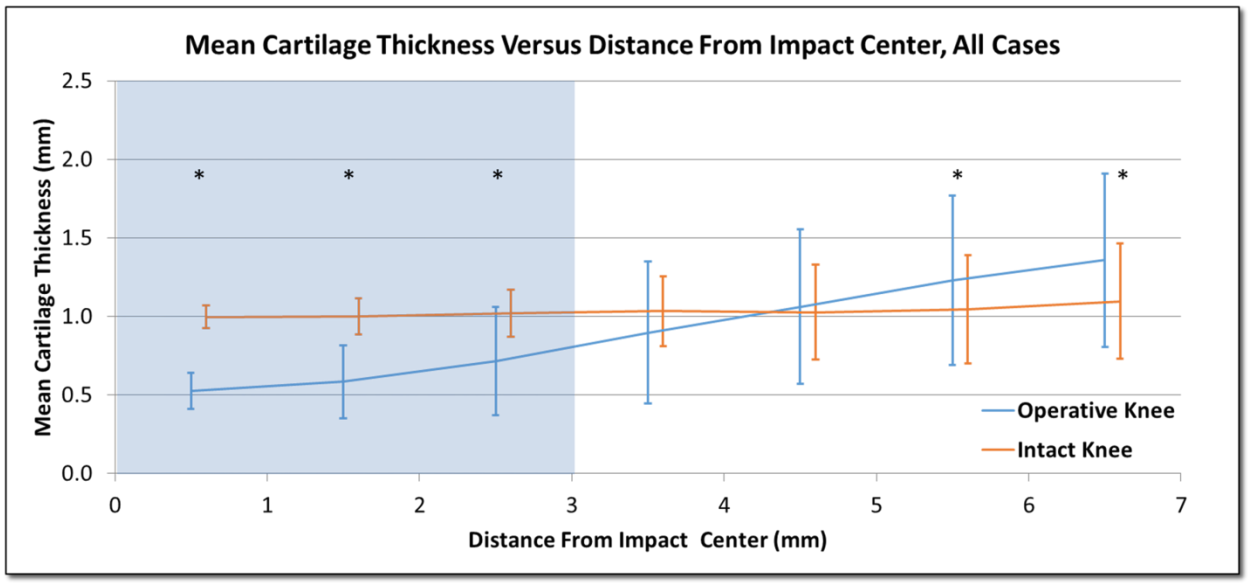

Figure 4-19 Average cartilage thickness versus distance from the center of impact. Asterisks indicate statistical significance ($p<0.05$). The impact zone has been demarcated in blue. Note that cartilage was significantly thinner in the operative knee within the impact zone. Significant differences in thickness at greater than 5-mm from the impact centroid may be attributable to right-left differences in surface geometry.

To confirm the findings of MRI, equivalent measures of gold standard micro CT were compared derived from MRI by sampling at the impact locations in the weight bearing cartilage. The results of this analysis are depicted in Table 4-3. Although statistically significant MRI-micro CT differences were evident in both operative and non-operative measurements, note that the mean difference between these measures was less than a single voxel of MRI resolution. This serves to verify the utility of MRI for measuring cartilage thickness, at least to within the accuracy presented here.

Table 4-3 Weight-bearing cartilage thickness measures: MRI vs. microCT

Weight-bearing (WB) Thickness Measure	Operative Knee*	Intact Knee+
MRI	1.18 ± 0.46 mm	1.04 ± 0.34 mm
microCT	1.56 ± 0.43 mm	1.2 ± 0.45 mm
Difference#	-0.38 ± 0.31 mm	-0.20 ± 0.18 mm

* MRI vs. microCT: p < 0.001
+ MRI vs. microCT: p < 0.001
# Operative vs. intact: p = 0.04

4.6 Discussion

This primary aim of this work was to establish the diagnostic capacity of clinical MRI sequences to identify early features predicative of osteoarthritis risk. To investigate this, an animal model was developed. Evidence of cartilage thinning at the time of euthanasia would serve as evidence of end stage OA, allowing for the correlation of imaging markers with the time to disease onset as established by imaging at intermediate time points. Cartilage thickness measures at time of euthanasia did not indicate that gross cartilage thinning had occurred.

Secondly, this work hypothesized that the time course of osteoarthritis correlated with injury severity. Without an adequate measure of end stage OA, it is impossible to answer this question at the present time. Despite this outcome, there were significant differences between cartilage that had been impacted and that which had not, suggesting that the impact itself had successfully damaged the articular cartilage within the impact zone. Based on the literature, it is reasonable to infer that this lesion would eventually initiate the onset of cartilage thinning.

CHAPTER 5: DISCUSSION AND CONCLUSION

5.1 Project summary

Post-traumatic osteoarthritis involves progressive and deleterious articular cartilage breakdown in response to acute joint injury. Time of injury represents a known point of disease initiation, from which the etiology and natural history of osteoarthritis may be studied. Within this more controlled environment, treatments to forestall or prevent the onset of PTOA may be devised. Diagnostic imaging plays a crucial role in this process by identifying relevant features of disease which may be tracked over time.

Large animal models facilitate the examination of clinically relevant joint injuries over time in order to elucidate features that are predicative of PTOA. Human equivalent joint size and cartilage thickness make goat knees a compelling environment in which to perform clinically relevant diagnostic imaging and evaluate new treatments. While somewhat less common in the literature than other large animal models, such as sheep, goats are an established vehicle for the modeling and study of osteoarthritis. [108]

Previous work has established the potential of MRI as a diagnostic tool for imaging OA. Previous work both at this and other institutions has demonstrated the capacity of MRI to non-invasively identify morphometric and compositional features of traumatic injury and possible markers of progressive disease. [102, 109] That previous work has also demonstrated the extensibility of imaging-derived measures from a research setting into a clinical setting. [109] However, that previous work has not fully explored the use of MRI diagnostic techniques to evaluate the entire history of disease from traumatic onset through PTOA progression to establish efficacy in a translatable preclinical model.

The purpose of the present work was to model acute cartilage injury, and correlate imaging findings to end-stage osteoarthritic changes. We hypothesized that imaging abnormalities would correlate with the rate of PTOA onset and progression. Our hope was that these features, evident on imaging in the immediate aftermath of joint injury, could be implemented as a clinical screening tool to identify patients that were likely to develop progressive PTOA. Identifying these patients closer to the time of initial joint injury may inform treatments and ultimately improve patient outcomes.

To investigate this hypothesis, partial meniscectomy and blunt cartilage impact injuries were implemented in a goat model of PTOA. This model was given a time course of 6 months in duration under the assumption that end-stage OA would present within or before the conclusion of the study. Impact groups of 0 J, 0.6 J, and 1.2 J were established under the assumption that the timing of onset and progression of PTOA are reliably predictable and determined by injury severity (i.e. higher energy injuries lead to earlier disease onset). Clinical MRI was used to record diagnostic and morphological information before and at intermediate time points after surgically induced injury.

Morphometric data acquired at the end point of the study presented measureable cartilage degradation within the area that had received blunt impact trauma, but little evidence to support cartilage thinning. To ensure that this was a negative result of the model – and not the result of imaging artifact or modeling error– we repeated our methods to calculate cartilage thickness using micro CT as a gold standard. Despite demonstrating the accuracy of MRI to within one voxel of accuracy, micro CT analysis of the cartilage samples produced similar results.

5.2 Discussion of limitations in the presented work

In order for imaging-based features identified as possible predictors of OA to be verified, a model must ultimately provide biochemical and/or morphometric evidence of late-stage OA. Without definitively establishing end-stage disease, there is no empirical way to conclude whether any of the identified imaging features were actually predictive of disease. To establish end-stage disease in the goat model 6 months after the injury that was induced, morphometric images acquired at time of sacrifice were analyzed to extract measures of cartilage thickness. Unfortunately, the results of this cartilage thickness analysis did not support the conclusion that end-stage OA was present at time of animal euthanasia. While morphometric MRI did identify significant differences between cartilage thickness at the point of impact and cartilage thickness from an equivalent location on the intact knee, this damage was local and appeared to be less an indication of whole joint cartilage thinning than evidence of damage directly related to the procedure itself. It can therefore be concluded that the surgical methods were of insufficient severity to induce PTOA in the goat in the prescribed timeframe.

In 2010, Little et al. completed a comprehensive review of the available literature describing goat models of osteoarthritis. [84] This work was completed as part of the OARSI histopathology initiative and was one of a series of articles detailing recommendations for animal OA research. Of the goat studies cited, Murphy et al. was the only one that successfully demonstrated the onset of end-stage OA. [110] A combination of ACL resection paired with medial meniscectomy was able to produce cartilage erosion in a time course of 6 months. Based on our results, it can be reasonably inferred that the injury severity of our partial meniscectomy and blunt impact was of reduced magnitude compared to that resulting from full medial meniscectomy paired with ACL resection. From a biomechanical standpoint, this is a reasonable

conclusion; although the overall load distributing capacity of the meniscus had been compromised after partial meniscectomy, a substantial amount of tissue remained in the joint. The intact medial and posterior meniscal attachments to bone and support provided by the surrounding joint ligaments likely preserved joint stability and some meniscal weight distributing capacity. Unfortunately, while the goat model used in the present work may have been on a trajectory towards OA, that the time course to disease was greater than 6 months.

A second goat study cited in Little's paper described a negative result to achieve end-stage OA eight months following medial meniscectomy. Measurements of contact stress and area at 4 and 8 months indicated that bony remodeling had actually served to reduce peak load and increase area as the study continued. [73] This finding is important because (1) the overloading effects of meniscectomy were reduced during the study course and (2) this model failed to result in articular cartilage degeneration representative of OA, despite full removal of the medial meniscus. In theory, a PTOA study of longer duration increases the ease with which the time course of injuries of differing severity may be studied. However, this study provides evidence that studies that are too long in duration may introduce additional variables such as bony remodeling or recovery which may confound the predictability of features of disease which might be identified and tracked longitudinally.

Therefore, a critical question arises: what modifications to the present study design would have yielded changes in cartilage morphometry consistent with end-stage OA at 6 months? It is likely that a more severe initial injury incorporating both meniscal injuries and ACL transection [110], in combination with the blunt impact methodology developed during this study, may have resulted in the predictable onset of end-stage OA in a period of 6 months or less.

5.3 Future opportunities for the longitudinal study of PTOA *in vivo*

Classically, MRI has been the standard of 3D morphometric and compositional visualization of joint tissues, whereas CT has been limited to bone. The development of contrast agents that can be used *in vivo* offers an opportunity to utilize the improved resolution of CT imaging for cartilage. [111, 112] Most of the contrast-enhanced CT work thus far has been performed *ex vivo* with a variety of human and animal cartilage explants or performed *in vivo* with mice. [45, 113, 114] However, a number of recent studies have performed contrast-enhanced CT in living human patients. Preliminary imaging findings in one identified a correlation between signal intensity and sulphated glycosaminoglycan (sGAG), one of the earliest cartilage molecules to degenerate with the onset of OA. [115] In another, a correlation between bone mineral density and cartilage lesion severity was identified. [116]

Although animal research has an established role for studying specific aspects of disease, the bulk of this research is performed as a substitute for directly studying the pathophysiology of human disease. The need for animal models stems from many reasons, including between-patient genetic variability, availability for follow-up testing, and ethical concerns. For the study of the onset and progression of PTOA *in vivo*, a major hurdle is a shortage of pre-injury imaging data to inform the underlying basis of post-injury features of trauma and disease. The problem is essentially that diagnostic and morphometric imaging is expensive, and that it is impractical to incorporate imaging into annual check-ups or other visits to the clinic without a background of joint pain or previous injury. Fortunately, the longitudinal study of PTOA need not be implemented on the entire healthy population in order to provide insights into the underlying mechanisms of disease. For example, athletes and soldiers have a markedly heightened risk of ACL rupture compared with the general population. Conducting pre-injury imaging screens on

individuals without a history of traumatic joint injury from these groups could offer tremendous opportunities for follow-up diagnostic imaging in the event that they were to sustain injuries at a later time. Such a clinical research study has been performed with movement screening as the diagnostic method. [117, 118] To this author's knowledge, this study design has not been performed with cross-sectional diagnostic imaging.

5.4 Conclusion

In summary, osteoarthritis is a debilitating disease with significant co-morbidities that exacts a significant financial and human toll on the health and welfare of Americans today. OA patients present to the clinic with symptoms at an advanced, irreversible state in the disease process. At this point, treatment options to preserve the native joint are limited. Identification of at-risk patients earlier paired with novel treatments grounded in an evidence-based understanding of the disease have the potential to both forestall the onset of debilitative symptoms and prevent to development of the disease altogether. Although the model developed in this work did not result in cartilage thinning within the desired timeframe, multi-modal image analysis reaffirmed the diagnostic capability of MRI to identify clinically relevant features earlier than conventional diagnostic tools. It is this author's hope that continued advancement of MRI techniques paired with increased scanner availability and reductions in cost will provide the necessary incentive to finally replace radiography as the clinical standard for diagnosing OA within the next ten years.

REFERENCES

1. Yelin, E., S. Weinstein, and T. King, *The burden of musculoskeletal diseases in the United States*. 2016. p. 259-260.

2. Weinstein, S., et al. . *The Burden of Musculoskeletal Diseases in the United States*. 2017; Available from: http://www.boneandjointburden.org.

3. Kuettner KE, G.V., *Osteoarthritic Disorders.* 1995: p. xxi-xxv.

4. NIAMS. *Handout on Health: Osteoarthritis*. 2016 [cited 2017 April 18]; Available from: https://www.niams.nih.gov/Health_Info/Osteoarthritis/default.asp.

5. Chu, C.R., et al., *Early diagnosis to enable early treatment of pre- osteoarthritis.* Arthritis Research & Therapy, 2012. **14**(3): p. 212-212.

6. Lawrence, R.C., et al., *Estimates of the prevalence of arthritis and other rheumatic conditions in the United States: Part II.* Arthritis & Rheumatism, 2008. **58**(1): p. 26-35.

7. Suri, P., D.C. Morgenroth, and D.J. Hunter, *Epidemiology of osteoarthritis and associated comorbidities.* PM & R : the journal of injury, function, and rehabilitation, 2012. **4**(5 Suppl): p. S10.

8. Whittaker, J.L., et al., *Evidence of early post- traumatic osteoarthritis and other negative health outcomes 3-10 years following knee joint injury in youth sport*. 2015. p. A180-A181.

9. Center, U.o.M.M. *Osteoarthritis*. 2012 [cited 2017 April 25]; Available from: http://www.umm.edu/health/medical/reports/articles/osteoarthritis.

10. Anderson, D.D., et al., *Post-Traumatic Osteoarthritis: Improved Understanding and Opportunities for Early Intervention.* Journal of Orthopaedic Research, 2011. **29**(6): p. 802-809.

11. Brown, T.D., et al., *Posttraumatic osteoarthritis: A first estimate of incidence, prevalence, and burden of disease.* Journal of Orthopaedic Trauma, 2006. **20**(10): p. 739-744.

12. Roos, E., *Joint injury causes knee osteoarthritis in young adults.* Current Opinion In Rheumatology, 2005. **17**(2): p. 195-200.

13. Whittaker, J.L., et al., *Outcomes associated with early post- traumatic osteoarthritis and other negative health consequences 3- 10 years following knee joint injury in youth sport.* Osteoarthritis and Cartilage, 2015. **23**(7): p. 1122.

14. Rivera, J.C., et al., *Posttraumatic osteoarthritis caused by battlefield injuries: the primary source of disability in warriors.* The Journal of the American Academy of Orthopaedic Surgeons, 2012. **20 Suppl 1**: p. S64.

15. Saltzman, C.L., et al., *Epidemiology of ankle arthritis: report of a consecutive series of 639 patients from a tertiary orthopaedic center.* The Iowa orthopaedic journal, 2005. **25**: p. 44-46.

16. Brophy, R.H., et al., *Total Knee Arthroplasty After Previous Knee Surgery.* Journal of Bone and Joint Surgery-American Volume, 2014. **96A**(10): p. 801-805.

17. Lunebourg, A., et al., *Lower function, quality of life, and survival rate after total knee arthroplasty for posttraumatic arthritis than for primary arthritis.* Acta Orthopaedica, 2015. **86**(2): p. 189-194.

18. Hepp, P., et al., *[Total knee arthroplasty in post-traumatic osteoarthritis].* Z Orthop Unfall, 2012. **150**(4): p. 374-80.

19. Larson, A., A. Hanssen, and J. Cass, *Does Prior Infection Alter the Outcome of TKA After Tibial Plateau Fracture?* Clin Orthop Relat Res, 2009. **467**(7): p. 1793-1799.

20. Bergeron, M.F., et al., *International Olympic Committee consensus statement on youth athletic development.* British Journal of Sports Medicine, 2015. **49**(13): p. 843-851.

21. Emery, C.A., W.H. Meeuwisse, and J.R. McAllister, *Survey of sport participation and sport injury in calgary and area high schools.* Clinical Journal of Sport Medicine, 2006. **16**(1): p. 20-26.

22. Vos, T., et al., *Years lived with disability (YLDs) for 1160 sequelae of 289 diseases and injuries 1990– 2010: a systematic analysis for the Global Burden of Disease Study 2010.* The Lancet, 2012. **380**(9859): p. 2163-2196.

23. Giannoudis, P.V., et al., *Articular step- off and risk of post- traumatic osteoarthritis. Evidence today.* Injury, 2010. **41**(10): p. 986-995.

24. Weigel, D. and J. Marsh, *High- energy fractures of the tibial plateau: Knee function after longer follow-up.* Journal of Bone and Joint Surgery, 2002. **84**(9): p. 1541-51.

25. Olson, S., *Post-Traumatic Arthritis Pathogenesis, Diagnosis and Management*, ed. F. Guilak and P. SpringerLink Content. 2015: Boston, MA : Springer US : Imprint: Springer.

26. *Special Issue: Injury and post-traumatic osteoarthritis.* J Orthop Res, 2017. **35**(3): p. 395-396.

27. Martin, K.R., et al., *Body mass index, occupational activity, and leisure-time physical activity: an exploration of risk factors and modifiers for knee osteoarthritis in the 1946 British birth cohort.(Research article).* BMC Musculoskeletal Disorders, 2013. **14**: p. 219.

28. Gelber, A.C., et al., *Joint injury in young adults and risk for subsequent knee and hip osteoarthritis.* Annals of internal medicine, 2000. **133**(5): p. 321.

29. Altman, R., et al., *Development of criteria for the classification and reporting of osteoarthritis: Classification of osteoarthritis of the knee.* Arthritis & Rheumatism, 1986. **29**(8): p. 1039-1049.

30. Peat, G., et al., *Clinical classification criteria for knee osteoarthritis: performance in the general population and primary care.* Ann Rheum Dis, 2006. **65**(10): p. 1363.

31. Guermazi, A., et al., *Different thresholds for detecting osteophytes and joint space narrowing exist between the site investigators and the centralized reader in a multicenter knee osteoarthritis study— data from the Osteoarthritis Initiative.* Skeletal Radiol, 2012. **41**(2): p. 179-186.

32. Hawker, G.A., et al., *Measures of adult pain: Visual Analog Scale for Pain (VAS Pain), Numeric Rating Scale for Pain (NRS Pain), McGill Pain Questionnaire (MPQ), Short-Form McGill Pain Questionnaire (SF-MPQ), Chronic Pain Grade Scale (CPGS), Short Form-36 Bodily Pain Scale (SF-36 BPS), and Measure of Intermittent and Constant Osteoarthritis Pain (ICOAP.* Arthritis Care & Research, 2011. **63**(S11): p. S240-S252.

33. Tegner, Y. and J. Lysholm, *Rating systems in the evaluation of knee ligament injuries.* Clinical Orthopaedics and Related Research, 1985. **198**: p. 43-49.

34. Bellamy, N., et al., *Validation study of WOMAC: a health status instrument for measuring clinically important patient relevant outcomes to antirheumatic drug therapy in patients with osteoarthritis of the hip or knee.* J Rheumatol, 1988. **15**(12): p. 1833-40.

35. Roos, E.M. and L.S. Lohmander, *The Knee injury and Osteoarthritis Outcome Score (KOOS): from joint injury to osteoarthritis.* Health and Quality of Life Outcomes, 2003. **1**: p. 64-64.

36. Duffell, L.D., et al., *Balance and gait adaptations in patients with early knee osteoarthritis().* Gait Posture, 2014. **39**(4): p. 1057-61.

37. Sharma, L., et al., *Varus and Valgus Alignment and Incident and Progressive Knee Osteoarthritis.* Ann Rheum Dis, 2010. **69**(11): p. 1940-5.

38. Subotnick, S.I., *Limb Length Discrepancies of the Lower Extremity (The Short Leg Syndrome).* J Orthop Sports Phys Ther, 1981. **3**(1): p. 11-16.

39. Solomon, L., *Patterns of osteoarthritis of the hip.* J Bone Joint Surg Br, 1976. **58**(2): p. 176-83.

40. Tallroth, K., et al., *Preoperative leg- length inequality and hip osteoarthrosis: a radiographic study of 100 consecutive arthroplasty patients.* Skeletal Radiol, 2005. **34**(3): p. 136-139.

41. Gofton, J.P. and G.E. Trueman, *Studies in osteoarthritis of the hip. II. Osteoarthritis of the hip and leg-length disparity.* Can Med Assoc J, 1971. **104**(9): p. 791-9.

42. Botter, S.M., et al., *Quantification of subchondral bone changes in a murine osteoarthritis model using micro-CT.* Biorheology, 2006. **43**(3-4): p. 379-88.

43. Bouxsein, M.L., et al., *Guidelines for assessment of bone microstructure in rodents using micro–computed tomography*. 2010: Hoboken. p. 1468-1486.

44. Xie, L., et al., *Quantitative assessment of articular cartilage morphology via EPIC-mu CT.* Osteoarthritis and Cartilage, 2009. **17**(3): p. 313-320.

45. Borges, P.D., et al., *Rapid, automated imaging of mouse articular cartilage by microCT for early detection of osteoarthritis and finite element modelling of joint mechanics.* Osteoarthritis and Cartilage, 2014. **22**(10): p. 1419-1428.

46. Guermazi, A., et al., *Prevalence of abnormalities in knees detected by MRI in adults without knee osteoarthritis: population based observational study (Framingham Osteoarthritis Study).* BMJ : British Medical Journal, 2012. **345**.

47. Eckstein, F., et al., *Magnetic resonance imaging (MRI) of articular cartilage in knee osteoarthritis (OA): morphological assessment.* Osteoarthritis and cartilage, 2006. **14 Suppl A**: p. A46.

48. Guermazi, A., et al., *Unresolved Questions in Rheumatology: Motion for Debate: Osteoarthritis Clinical Trials Have Not Identified Efficacious Therapies Because Traditional Imaging Outcome Measures Are Inadequate.* Arthritis & Rheumatism, 2013. **65**(11): p. 2748-2758.

49. Eckstein, F., et al., *Relationship of compartment- specific structural knee status at baseline with change in cartilage morphology: a prospective observational study using data from the osteoarthritis initiative.* Arthritis Research & Therapy, 2009. **11**(3): p. R90-R90.

50. Peterfy, C.G., et al., *MRI protocols for whole- organ assessment of the knee in osteoarthritis.* Osteoarthritis And Cartilage, 2006. **14**: p. A95-A111.

51. Peterfy, C.G., et al., *Whole- Organ Magnetic Resonance Imaging Score (WORMS) of the knee in osteoarthritis.* Osteoarthritis and Cartilage, 2004. **12**(3): p. 177-190.

52. Carballido-Gamio, J., et al., *Inter- subject comparison of MRI knee cartilage thickness.* Medical Image Analysis, 2008. **12**(2): p. 120-135.

53. Eckstein, F., et al., *Long- term and resegmentation precision of quantitative cartilage MR imaging (qMRI).* Osteoarthritis and Cartilage, 2002. **10**(12): p. 922-928.

54. Kroon, D.-J., et al. *MRI based knee cartilage assessment*. 2012.

55. Eckstein, F., et al., *Imaging of cartilage and bone: promises and pitfalls in clinical trials of osteoarthritis.* Osteoarthritis and Cartilage, 2014. **22**(10): p. 1516-1532.

56. McKinley, O.T., et al., *Basic Science of Intra- articular Fractures and Posttraumatic Osteoarthritis.* Journal of Orthopaedic Trauma, 2010. **24**(9): p. 567-570.

57. Sinusas, K. *Osteoarthritis: Diagnosis and Treatment*. 2012 [cited 2017 March 28].

58. Hochberg, M.C., et al., *American College of Rheumatology 2012 recommendations for the use of nonpharmacologic and pharmacologic therapies in osteoarthritis of the hand, hip, and knee.* Arthritis care & research, 2012. **64**(4): p. 465.

59. Scott, D.L., et al., *The clinical management of rheumatoid arthritis and osteoarthritis: strategies for improving clinical effectiveness.* Rheumatology, 1998. **37**(5): p. 546-554.

60. Lauder, T.D., et al., *Sports and physical training injury hospitalizations in the Army.* American Journal of Preventive Medicine, 2000. **18**(3): p. 118-128.

61. Lohmander, L., et al., *The long- term consequence of anterior cruciate ligament and meniscus injuries - Osteoarthritis*, in *Am. J. Sports Med.* 2007. p. 1756-1769.

62. Lohmander, L.S., et al., *High prevalence of knee osteoarthritis, pain, and functional limitations in female soccer players twelve years after anterior cruciate ligament injury.* Arthritis and Rheumatism, 2004. **50**(10): p. 3145-3152.

63. Cameron, K.L., et al., *Normative Values for the KOOS and WOMAC in a Young Athletic Population.* The American Journal of Sports Medicine, 2013. **41**(3): p. 582-589.

64. Holm, I., et al., *No Differences in Prevalence of Osteoarthritis or Function After Open Versus Endoscopic Technique for Anterior Cruciate Ligament Reconstruction.* The American Journal of Sports Medicine, 2012. **40**(11): p. 2492-2498.

65. Owens, D.B., et al., *Combat Wounds in Operation Iraqi Freedom and Operation Enduring Freedom.* The Journal of Trauma: Injury, Infection, and Critical Care, 2008. **64**(2): p. 295-299.

66. Schreiber, A.M., et al., *A Comparison Between Patients Treated at a Combat Support Hospital in Iraq and a Level I Trauma Center in the United States.* The Journal of Trauma: Injury, Infection, and Critical Care, 2008. **64**(2 Suppl): p. S118-S122.

67. Cross, J.D., et al., *Battlefield Orthopaedic Injuries Cause the Majority of Long-term Disabilities.* Journal Of The American Academy Of Orthopaedic Surgeons, 2011. **19**: p. S1-S7.

68. Gratz, K.R., et al., *The Effects of Focal Articular Defects on Cartilage Contact Mechanics.* Journal of Orthopaedic Research, 2009. **27**(5): p. 584-592.

69. Jones, H., et al., *Meniscal and Chondral Loss in the Anterior Cruciate Ligament Injured Knee.* Sports Med, 2003. **33**(14): p. 1075-1089.

70. Seitz, A.M., et al., *Effect of partial meniscectomy at the medial posterior horn on tibiofemoral contact mechanics and meniscal hoop strains in human knees.* Journal of Orthopaedic Research, 2012. **30**(6): p. 934-942.

71. Heckelsmiller, D.J., et al., *Changes in Joint Contact Mechanics in a Large Quadrupedal Animal Model after Focal and Whole-Joint Soft Tissue Injury.* Journal of Biomechanical Engineering, 2017.

72. von Lewinski, G., et al., *Experimental measurement of tibiofemoral contact area in a meniscectomized ovine model using a resistive pressure measuring sensor.* Annals of Biomedical Engineering, 2006. **34**(10): p. 1607-1614.

73. Bylski-Austrow, D.I., et al., *Knee joint contact pressure decreases after chronic meniscectomy relative to the acutely meniscectomized joint: A mechanical study in the goat.* Journal of Orthopaedic Research, 1993. **11**(6): p. 796-804.

74. Kilcoyne, C., et al., *Epidemiology of Meniscal Injury Associated With ACL Tears in Young Athletes.* Orthopedics, 2012. **35**(3): p. 208-212.

75. Curl, W.W., et al., *Cartilage injuries: A review of 31,516 knee arthroscopies.* Arthroscopy: The Journal of Arthroscopic and Related Surgery, 1997. **13**(4): p. 456-460.

76. Widuchowski, W., J. Widuchowski, and T. Trzaska, *Articular cartilage defects: Study of 25,124 knee arthroscopies.* The Knee, 2007. **14**(3): p. 177-182.

77. Gudas, R., et al., *A Prospective Randomized Clinical Study of Mosaic Osteochondral Autologous Transplantation Versus Microfracture for the Treatment of Osteochondral Defects in the Knee Joint in Young Athletes.* Arthroscopy: The Journal of Arthroscopic and Related Surgery, 2005. **21**(9): p. 1066-1075.

78. Hjelle, K., et al., *Articular cartilage defects in 1,000 knee arthroscopies.* Arthroscopy-the Journal of Arthroscopic and Related Surgery, 2002. **18**(7): p. 730-734.

79. Cicuttini, F., et al., *Association of cartilage defects with loss of knee cartilage in healthy, middle- age adults: a prospective study.* Arthritis and rheumatism, 2005. **52**(7): p. 2033.

80. Sniekers, Y.H., et al., *Animal models for osteoarthritis: the effect of ovariectomy and estrogen treatment – a systematic approach.* Osteoarthritis and Cartilage, 2008. **16**(5): p. 533-541.

81. Bendele, A.M. and J.F. Hulman, *Effects of body weight restriction on the development and progression of spontaneous osteoarthritis in guinea pigs.* Arthritis and rheumatism, 1991. **34**(9): p. 1180.

82. Hyttinen, M., et al., *Age matters: collagen birefringence of superficial articular cartilage is increased in young guinea-pigs but decreased in older animals after identical physiological type of joint loading.* Osteoarthritis And Cartilage, 2001. **9**(8): p. 694-701.

83. Gregory, M.H., et al., *A Review of Translational Animal Models for Knee Osteoarthritis.* 2012. **2012**.

84. Little, C.B., et al., *The OARSI histopathology initiative - recommendations for histological assessments of osteoarthritis in sheep and goats.* Osteoarthritis Cartilage, 2010. **18**: p. S80-S92.

85. Laurent, D., et al., *In vivo MRI of cartilage pathogenesis in surgical models of osteoarthritis.* Skeletal Radiology, 2006. **35**(8): p. 555-564.

86. Oakley, S.P., et al., *Arthroscopy -- a potential gold standard for the diagnosis of the chondropathy of early osteoarthritis.* Osteoarthritis and cartilage, 2005. **13**(5): p. 368.

87. Rorvik, A.M. and J. Teige, *Unstable stifles without clinical or radiographic osteoarthritis in young goats: an experimental study.* Acta Vet Scand, 1996. **37**(3): p. 265-72.

88. Ghosh, P., et al., *The influence of weight-bearing exercise on articular cartilage of meniscectomized joints. An experimental study in sheep.* Clin Orthop Relat Res, 1990(252): p. 101-13.

89. Armstrong, S.J., et al., *Moderate exercise exacerbates the osteoarthritic lesions produced in cartilage by meniscectomy: a morphological study.* Osteoarthritis Cartilage, 1993. **1**(2): p. 89-96.

90. Beveridge, J.E., N.G. Shrive, and C.B. Frank, *Meniscectomy causes significant in vivo kinematic changes and mechanically induced focal chondral lesions in a sheep model.* J Orthop Res, 2011. **29**(9): p. 1397-405.

91. Pedersen, D.R., et al., *Bone contusion progression from traumatic knee injury: association of rate of contusion resolution with injury severity.* Open Access Journal of Sports Medicine, 2017. **8**: p. 9-15.

92. Burgin, L.V. and R.M. Aspden, *A drop tower for controlled impact testing of biological tissues.* Medical Engineering & Physics, 2007. **29**(4): p. 525-530.

93. Bonnevie, E.D., et al., *Characterization of Tissue Response to Impact Loads Delivered Using a Hand-Held Instrument for Studying Articular Cartilage Injury.* 2015. **6**(4): p. 226-232.

94. Diestelmeier, B.W., et al., *An Instrumented Pendulum System for Measuring Energy Absorption During Fracture Insult to Large Animal Joints in Vivo.* Journal of Biomechanical Engineering-Transactions of the Asme, 2014. **136**(6): p. 5.

95. Bolam, C.J., et al., *Characterization of experimentally induced post-traumatic osteoarthritis in the medial femorotibial joint of horses.* American Journal of Veterinary Research, 2006. **67**(3): p. 433-447.

96. Brown, T.D., et al., *Effects of osteochondral defect size on cartilage contact stress.* Journal of Orthopaedic Research, 1991. **9**(4): p. 559-567.

97. Patel, P.S.D., D.E.T. Shepherd, and D.W.L. Hukins, *Compressive properties of commercially available polyurethane foams as mechanical models for osteoporotic human cancellous bone.* Bmc Musculoskeletal Disorders, 2008. **9**.

98. Taylor, W.R., et al., *Tibio- femoral joint contact forces in sheep.* Journal of Biomechanics, 2006. **39**(5): p. 791-798.

99. Elsner, J.J., et al., *Meniscal implant biomechanical performance: a novel quantitative approach.* Proceedings of the Asme Summer Bioengineering Conference - 2009, Pt a and B, 2009: p. 875-876.

100. Brown, T.D., M.J. Rudert, and N.M. Grosland, *New methods for assessing cartilage contact stress after articular fracture.* Clinical orthopaedics and related research, 2004(423): p. 52.

101. Guettler, J.H., et al., *Osteochondral deflects in the human knee - Influence of defect size on cartilage rim stress and load redistribution to surrounding cartilage.* American Journal of Sports Medicine, 2004. **32**(6): p. 1451-1458.

102. Klocke, N.F., et al., *Comparison of T1 rho, dGEMRIC, and Quantitative T2 MRI in Preoperative ACL Rupture Patients.* Academic Radiology, 2013. **20**(1): p. 99-107.

103. Siemens. *6-Channel Body Coil*. [cited 2017 March 27]; Available from: https://usa.healthcare.siemens.com/magnetic-resonance-imaging/options-and-upgrades/coils/6-channel-body-coil.

104. Siemens. *Tx/Rx 15-Channel Knee Coil*. [cited 2017 March 27]; Available from: https://usa.healthcare.siemens.com/magnetic-resonance-imaging/options-and-upgrades/coils/tx-rx-15-channel-knee-coil.

105. Schneider, E., et al., *Equivalence and precision of knee cartilage morphometry between different segmentation teams, cartilage regions, and MR acquisitions.* Osteoarthritis and Cartilage, 2012. **20**(8): p. 869-879.

106. Bruker, m. *NRecon User Manual*. 2016 [cited 2017 March 27]; Available from: http://bruker-microct.com/next/NReconUserGuide.pdf.

107. Grood, E.S. and W.J. Suntay, *A Joint Coordinate System for the Clinical Description of Three-Dimensional Motions: Application to the Knee.* Journal of Biomechanical Engineering, 1983. **105**(2): p. 136-144.

108. Wilke, H.J., A. Kettler, and L.E. Claes, *Are sheep spines a valid biomechanical model for human spines?* Spine, 1997. **22**(20): p. 2365.

109. Klocke, N.F., *Characterizing cartilage-specific T1rho MRI for clinical translation and application*. 2011, University of Iowa.

110. Murphy, J.M., et al., *Stem cell therapy in a caprine model of osteoarthritis.* Arthritis & Rheumatism, 2003. **48**(12): p. 3464-3474.

111. Bansal, P.N., et al., *Cationic Contrast Agents Improve Quantification of Glycosaminoglycan (GAG) Content by Contrast Enhanced CT Imaging of Cartilage.* Journal of Orthopaedic Research, 2011. **29**(5): p. 704-709.

112. Joshi, N.S., et al., *Effect of contrast agent charge on visualization of articular cartilage using computed tomography: exploiting electrostatic interactions for improved sensitivity.* Journal of the American Chemical Society, 2009. **131**(37): p. 13234.

113. Lakin, B.A., et al., *Contrast-enhanced CT facilitates rapid, non-destructive assessment of cartilage and bone properties of the human metacarpal.* Osteoarthritis and Cartilage, 2015. **23**(12): p. 2158-2166.

114. Stewart, R.C., et al., *Contrast- enhanced CT with a high- affinity cationic contrast agent for imaging ex vivo bovine, intact ex vivo rabbit, and in vivo rabbit cartilage.* Radiology, 2013. **266**(1): p. 141.

115. van Tiel, J., et al., *Quantitative in vivo CT arthrography of the human osteoarthritic knee to estimate cartilage sulphated glycosaminoglycan content: correlation with ex-vivo reference standards.* Osteoarthritis Cartilage, 2016. **24**(6): p. 1012-20.

116. Myller, K.A., et al., *In Vivo Contrast-Enhanced Cone Beam CT Provides Quantitative Information on Articular Cartilage and Subchondral Bone.* 2017. **45**(3): p. 811-818.

117. Gwinn, D.E., et al., *The relative incidence of anterior cruciate ligament injury in men and women at the United States Naval Academy.* American Journal of Sports Medicine, 2000. **28**(1): p. 98-102.

118. Beutler, A.I., et al., *Muscle strength and qualitative jump-landing differences in male and female military cadets: The jump-ACL study.* Journal of Sports Science and Medicine, 2009. **8**(4): p. 663-671.

APPENDICES

Appendix A: Micro CT Reconstruction Log

```
[System]
Scanner=SkyScan1176
Instrument S/N=13G08091
Hardware version=A
Software=Version 1. 1 (build 10)
Home directory=C:\SkyScan1176
Source Type=PANalytical's Microfocus Tube
Camera=Princeton Instruments
Camera Pixel Size (um)=   12.61
CameraXYRatio=0.9990
Bed shift in X per 1000 lines=0.661000
Bed shift in Y per 1000 lines=-3.938000
[Acquisition]
Data directory=E:\CORT-2\50002-L\FEM-MED
Filename Prefix=G50002L FEM MED
Filename Index Length=4
Number of Files=  659
Source Voltage (kV)=  80
Source Current (uA)= 313
Number of Rows= 2672
Number of Columns= 4000
Image crop origin X=   0
Image crop origin Y=0
Camera binning=1x1
Image Rotation=0.4200
Gantry direction=CC
Number of connected scans=3
Number of lines to be reconstructed=1557
Image Pixel Size (um)=    8.85
Object to Source (mm)=117.185
Camera to Source (mm)=165.499
System Matrix Calibration=NO
Vertical Object Position (mm)=150.369
Optical Axis (line)=1333
Filter=Cu + Al
Image Format=TIFF
Data Offset (bytes)= 264
Horizontal overlap (pixel)=128
Camera horizontal position=Center
Depth (bits)=16
Visual Camera=OFF
Synchronised Scan=OFF
Delay for external event (ms)=(5)
List mode=OFF (2)
Screen LUT=0
Exposure (ms)=  1120
```

```
Rotation Step (deg)=0.300
Frame Averaging=ON (1)
Use 360 Rotation=NO
Geometrical Correction=ON
Camera Offset=OFF
Scanning Start Angle=0.000
Median Filtering=ON
Flat Field Correction=ON
Rotation Direction=CC
Scanning Trajectory=ROUND
User Name=
User Rights=full access
Type Of Motion=STEP AND SHOOT
Source Temperature=29.41 °C
Study Date and Time=Aug 18, 2016  18:31:42
Scan duration=00:33:20
Maximum vertical TS=5.0
[Reconstruction]
Reconstruction Program=NRecon
Program Version=Version: 1.6.10.4
Program Home Directory=R:\Ortho-Biomechanics\CORT-II_Rabbits-and-
Goats\Capra_Study\study_CT_contrast\Analysis Software\NRecon
Reconstruction engine=GPUReconServer
Engine version=Version: 1.6.10
Reconstruction from batch=Yes
Postalignment=-2.50
Connected Reconstruction (parts)=3
Sub-scan post alignment [0]=-0.500000
Sub-scan post alignment [1]=-3.000000
Sub-scan post alignment [2]=-2.500000
Sub-scan scan length [0]=1554
Sub-scan scan length [1]=1556
Sub-scan scan length [2]=1557
Used extra rotation per scan(deg)= 0.000  0.000  0.000
Used extra shift in X per scan(micron)= 0.000  13.090  17.898
Used extra shift in Y per scan(micron)= 0.000  31.112  27.123
Reconstruction servers= MEK012
Dataset Origin=SkyScan1176
Dataset Prefix=G50002L FEM MED ~02
Dataset Directory=\\agit8r.obrl.uiowa.edu\ct\uCT\CORT2\50002-L\FEM-MED
Output Directory=\\agit8r.obrl.uiowa.edu\ct\uCT\CORT2\50002-L\FEM-
MED\G50002L FEM MED _Rec
Time and Date=Aug 25, 2016  13:38:52
First Section=856
Last Section=4880
Reconstruction duration per slice (seconds)=2.091932
Total reconstruction time (3111 slices) in seconds=6508.000000
Section to Section Step=1
Sections Count=4025
Result File Type=BMP
Result File Header Length (bytes)=1134
Result Image Width (pixels)=4000
```

```
Result Image Height (pixels)=4000
Pixel Size (um)=8.85324
Reconstruction Angular Range (deg)=197.70
Use 180+=OFF
Angular Step (deg)=0.3000
Smoothing=4
Smoothing kernel=2 (Gaussian)
Ring Artifact Correction=10
Draw Scales=OFF
Object Bigger than FOV=OFF
Reconstruction from ROI=OFF
Filter cutoff relative to Nyquist frequency=100
Filter type=0
Filter type description=Hamming (Alpha=0.54)
Undersampling factor=1
Threshold for defect pixel mask (%)=0
Beam Hardening Correction (%)=15
CS Static Rotation (deg)=0.00
Minimum for CS to Image Conversion=-0.002658
Maximum for CS to Image Conversion=0.023627
HU Calibration=OFF
BMP LUT=0
Cone-beam Angle Horiz.(deg)=17.184624
Cone-beam Angle Vert.(deg)=11.527124
Automatic matching in Z=50
Automatic matching in X/Y=50
Automatic matching in rotation=5.000000
Automatic fusion=1
[File name convention]
Filename Index Length=4
Filename Prefix=G50002L FEM MED _rec
```